Thermo-elastic solid shell formulation with phase field fracture for thin-walled FGMs

P K Asur Vijaya Kumar[a,c,*], A. Dean[b,c], J. Reinoso[c], M. Paggi[a]

[a]*IMT School for Advanced Studies Lucca, Piazza San Francesco 19, 55100, Lucca, Italy*
[b]*School of Civil Engineering, College of Engineering, Sudan University of Science and Technology, P.O. Box 72, Khartoum, Sudan*
[c]*Elasticity and Strength of Materials Group, School of Engineering, University of Seville, Camino de los Descubrimientos s/n, 41092, Seville, Spain*

Abstract

Thermo-elastic fracture is a matter of important concern for thin-walled structures made of functionally graded materials (FGMs). Based on this practical relevance, a thermodynamically consistent framework is proposed in this investigation for solving the coupled thermo-mechanical phase-field fracture problem in thin-walled structures made of FGMs. The formulation of the current model is constructed via the evaluation of the phase-field in the Clausius-Duhem inequality leading in to first-order stability conditions in order to ensure thermodynamic consistency. The three-dimensional Kirchhoff-Saint-Venant constitutive model is modified to accommodate the functional grading in the material properties. The computational model is combined with Enhanced Assumed Strain (EAS) and Assumed Natural Strains (ANS) to alleviate locking pathology concerning the solid shell formulation, leading to a coupled non-linear variational formulation. Several benchmark examples (straight and curved shells) are examined to assess the model capabilities. Moreover, crack deflection, and temperature distributions in the FGM structures are compared with their homogeneous surrogates, to show the importance of the technological solutions with two or even three FGM phases.

Keywords: A. Solid Shell, B. Phase-Field Fracture, C. Finite Element Method, D: Non-linear thermo-elasticity, E: Functionally Graded Materials.

1. Introduction

Modern technological processes concerning aerospace, automotive, power, electronics, bio-engineering, demand materials that have mutually exclusive properties which are unobtainable using conventional materials. For example, gears must have a tough core to withstand fracture, but must be stiff and hard outside to prevent wear [1], or an ideal turbine blade consists of a tough core but high-temperature resistance and low melting point outside [2, 3]. Even though the concept of functionally graded materials (FGM) was initially proposed to mimic structures such as bones [4], bamboo trees [5], these materials found their place in the space industry [6], rocket engines [7], shell structures [8, 9], airplanes [10], to name a few. FGMs exhibit many advantages as compared to conventional materials by providing or combining the benefits of two different material via a gradual grading. They are often used to create thermal barriers [11] or connect two incompatible materials [12]. See [3] for a detailed review of the production, classification, and application of FGMs.

FGMs are shown to be fundamentally different from homogeneous materials [3] in terms of elastic and thermal responses. The material properties such as Young's modulus [13], fracture toughness [14], thermal properties of their homogeneous constituents behave differently, making the crack prediction difficult.

---

*Corresponding authors
Email address: `jreinoso@us.es` (J. Reinoso)

Computational methods such as FEM [15–17], XFEM [18–20], scaled boundary finite elements [21], isogeometric FEM [22], hybrid phase-field isogeometric analysis [23], isoparametric graded finite elements [24–26], cohesive zone models [27, 28], and many more have been used to study fracture events in FGMs.

Variational methods to fracture developed in the recent years constitute an effective tool for understanding nonlinear phenomena. Particularly, based on energy considerations, Phase-Field (PF) methods to fracture have emerged as powerful methods to deal with fracture initiation and propagation [29]. The PF approach has been applied to brittle materials [30], ductile materials [31–33], composites [34–41], hydrogen assisted cracking [42, 43], fatigue [44–47], to name a few of previous applications. The extension of these models to FGMs is discussed in [48, 49]. In this regard, Wu et al [50] conducted a detailed review of the phase-field. See [51–53] for efficient alternative formulations for phase-field crack. Within this context, thermo-mechanics coupled with PF models have been developed in recent years for various applications [54, 55], such as chemo-thermo-mechanical couplings [56], composite materials [33, 57].

Regarding the shell structures, many authors have proposed different approaches for their computation, as well as kinematic description such as XFEM [58–61], gradient enhanced damage methods [62–66], isoparametric shell analysis [67–69] using the classical shell theories such as the Kirchhoff-Love theory [70–73], or the Reissner-Mindlin theory [58, 60]. Recently, thermo-mechanical analysis of the solid shell with full integration with Enhanced Assumed Strains (EAS) and Assumed Natural Strain (ANS) to alleviate locking pathology has been discussed [74]. Moreover, the authors extended this idea to include the phase-field [9, 75]. A more detailed discussion on the application of thermo-mechanics models for shells can be found in [76] concerning the use of solid shells with reduced integration schemes at the element level.

This work presents a thermodynamically consistent phase-field modeling of fracture for thin-walled FGMs coupled with thermo-mechanics using the solid shell concept. The kinematic description of the body resembles that of the 8-node brick element [77–79] allowing to accommodate the constituent material model in three dimensions. Phase-field is introduced via Clausius-Duhem inequality leading to thermodynamic consistency and first-order optimality conditions consistent with [74]. Moreover, the Kirchhoff-Saint-Venant material law is modified to accommodate FGMs. Both elastic energy and thermal energy are degraded using same degradation function as in [80]. Specifically, the thermal energy degradation is achieved by degrading thermal conductivity. The potential locking deficiencies stemming from the shell complying with the low order kinematic displacement schemes are alleviated by combining EAS [81–85] and ANS schemes [86, 87], in line with [74, 88–91]. Furthermore, the coupling between thermal, phase-field and displacement fields concerning the EAS formulation are treated via static condensation of the enhancing stains at the element level [84], preserving the original size of the thermo-mechanical problem at the element level.

The article is organized as follows. Section 2 outlines the theoretical aspects of the coupled thermo-mechanical phase-field formulation in solid shells and the constitutive equations, focusing on thermodynamic consistency. Section 3 presents the finite element implementation of the model. Section 4 examines the numerical application of the proposed model to benchmark examples. The effect of grading in terms of crack path and load-bearing capacity is explored thoroughly. The thermo-mechanical interactions in the FGM are compared with the homogeneous materials response. The effect of temperature on the load-bearing capacity of the FGM structure is carefully analyzed. The impact of material properties such as Young's modulus, thermal conductivity, fracture energy on the FGM performance is examined using three different FGM pairs (metal-metal, ceramic-ceramic, ceramic-polymer). The model is then modified to accommodate a three-phase/ double FGM, and its thermo-elastic behavior is analyzed. Finally, the main conclusions of this article are drawn in Section 5.

2. Coupled thermo-mechanical formulation

2.1. Primary fields of thermo-mechanical analysis

Let $\mathcal{B}_0 \subset \mathbb{R}^n$ be a reference configuration of the n-dimensional Euclidean space with its delimiting boundary $\partial \mathcal{B}_0 \subset \mathbb{R}^{n-1}$. Define the displacement field $\mathbf{u}(\mathbf{X}, t) : \mathcal{B}_0 \times [0, t] \to \mathbb{R}^n$, temperature field $T(\mathbf{X}, t) : \mathcal{B}_0 \times [0, t] \to \mathbb{R}^+$, and the scalar damage (phase-field) $\mathfrak{d}(\mathbf{X}, t) : \mathcal{B}_0 \times [0, t] \to [0, 1]$ in the time interval $[0, t]$.
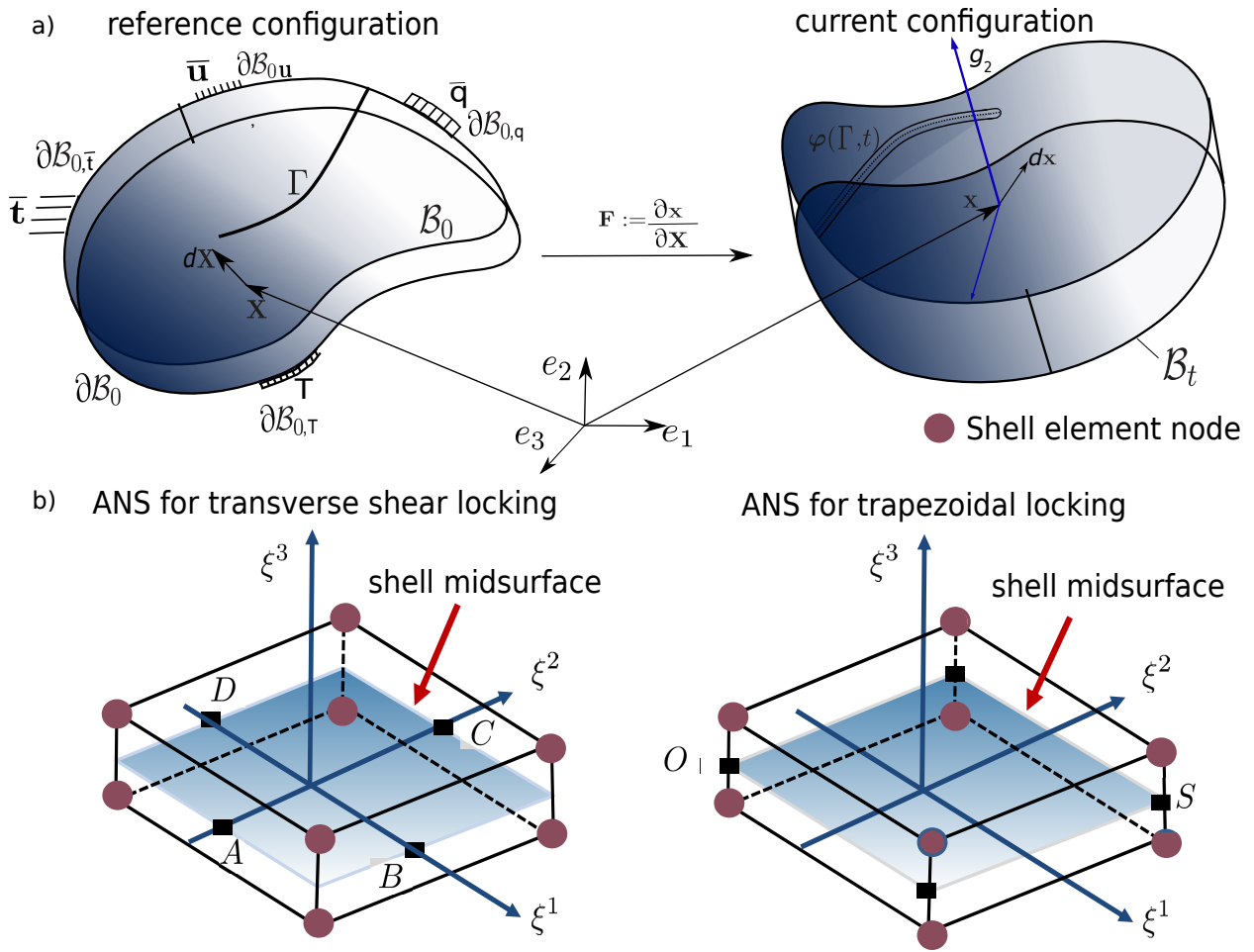
Figure 1: a) Finite deformation of a body: reference and current configurations. Deformation mapping $\boldsymbol{\varphi}(\mathbf{X}, t)$, that transforms at time t the reference configuration $\mathcal{B}_0$ onto the current configuration $\mathcal{B}_t$, and the displacement-derived deformation gradient $\mathbf{F}^u := \partial_{\mathbf{X}} \boldsymbol{\varphi}(\mathbf{X}, t)$. b) ANS for transverse shear locking and ANS for trapezoidal locking.

The external boundary $\partial \mathcal{B}_0$ is split into four parts $\partial \mathcal{B}_{0,\bar{t}}$, $\partial \mathcal{B}_{0,u}$, $\partial \mathcal{B}_{0,q}$, and $\partial \mathcal{B}_{0,T}$ such that $\partial \mathcal{B}_{0,u} \cap \partial \mathcal{B}_{0,\bar{t}} = \emptyset$, $\partial \mathcal{B}_{0,T} \cap \partial \mathcal{B}_{0,q} = \emptyset$, and $\partial \mathcal{B}_0 = \overline{\partial \mathcal{B}_{0,u} \cup \partial \mathcal{B}_{0,\bar{t}} \cup \partial \mathcal{B}_{0,T} \cup \partial \mathcal{B}_{0,q}}$.

The Dirichlet boundary conditions with respect to displacement and temperature, i.e boundary displacement $\bar{\mathbf{u}}$ and initial (reference) temperature T_0 are applied on $\partial \mathcal{B}_{0,u}$ and $\partial \mathcal{B}_{0,T}$ respectively. Meanwhile, Neumann boundary conditions in terms of traction $\bar{\mathbf{t}} = \boldsymbol{\sigma} \cdot \mathbf{n}(\mathbf{X}, t)$ and heat flux $\bar{q}$ can be applied on $\partial \mathcal{B}_{0,\bar{t}}$ and $\partial \mathcal{B}_{0,q}$, respectively, as shown in Fig. 1 for normal unit vector $\mathbf{n}$.

The phase-field approach to fracture can be interpreted as the competition between elastic energy (thermo-elastic) and the crack surface energy created due to the evolution of the scalar phase-field variable $\mathfrak{d}$. Within this context, assuming that the phase-field variable $\mathfrak{d}$ evolves from 0 (intact material) to 1 (fully damaged), the crack set Γ_t at any given time $[0, t]$ can be formulated as the following minimisation problem (see [30] for more details):

$$(\mathbf{u}^*, T^*, \Gamma_t) = \arg \min_{\mathcal{S}} \Pi(\mathbf{u}, T, \Gamma_t) = \arg \min_{\mathcal{S}} \left\{ \int_{\mathcal{B}_0 / \Gamma_t} \Psi(\mathbf{u}, T) \mathrm{d}\Omega + \int_{\Gamma_t} \mathcal{G}_C \mathrm{d}\Gamma \right\}, \tag{1}$$

with $\mathcal{S} = \{\mathbf{u} = \bar{\mathbf{u}} \text{ on } \partial \mathcal{B}_0, \ \Gamma_t \subseteq \Gamma_{t+1}\}$. Here, $\mathcal{G}_C$ represents the critical energy release rate, and $\Psi(\mathbf{u}, T)$ is the thermo-elastic strain energy density that depends on the material model. The total energy function in Eq. (1) is approximated as a free-discontinuous problem [92], owing to a smeared/diffusive crack representation using the scalar field $\mathfrak{d}$ of the sharp crack Γ. Under this approximation, the total energy takes the form:

$$\Pi(\mathbf{u}, \mathfrak{d}, T) = \int_{\mathcal{B}_0} g(\mathfrak{d}) \Psi_0(\mathbf{u}, T) \mathrm{d}\Omega + \int_{\mathcal{B}_0} \frac{\mathcal{G}_C}{4 c_w} \left[\frac{\alpha(\mathfrak{d})}{l} + l \left| \nabla \mathfrak{d} \right|^2 \right] \mathrm{d}\Omega + \Pi_{\text{ext}}. \tag{2}$$

Here, $c_w := \int_0^s \sqrt{\alpha(s)} \mathrm{d}s$ is the normalization parameter, $\alpha(\mathfrak{d})$ is the geometric crack function such that $\alpha(0) = 0$ and $\alpha(1) = 1$, and $g(\mathfrak{d}) : [0, 1] \to [1, 0]$ defines the degradation function of the initial thermo elastic energy. Naturally, such a degradation function is monotonically decreasing and satisfies $g(0) = 1$, $g(1) = 0$, and $\frac{dg}{d\mathfrak{d}} < 0$ in order to fulfill the thermodynamic consistency. The term $\Psi_0(\mathbf{u}, T)$ in Eq. (2) represents the initial thermo-elastic energy stemming from the material models, whose details are discussed in the sequel.

2.2. Solid shell formulation for thin walled structures

The key idea of the solid shell formulation with full integration is based on a locking free element which can alleviate transverse shear locking, volumetric locking, Poisson's locking and trapezoidal locking. Use of curvilinear co-ordinate system facilities the introduction of EAS and ANS parameter into the framework which in turn alleviates the locking pathology. The body under external forces undergoes deformation can be seen as a map $\boldsymbol{\varphi}(\mathbf{X}, t) : \mathcal{B}_0 \times [0, t] \to \mathbb{R}^3$ from reference material point $\mathbf{X} \in \mathcal{B}_0$ onto a current material point $\mathbf{x} \in \mathcal{B}_t$ in the current configuration $\mathcal{B}_t$ such that $\mathbf{x} = \boldsymbol{\varphi}(\mathbf{X}, t) = \mathbf{X} + \mathbf{u}(\mathbf{X}, t)$ for each t. The singular valued continuously differential function $\boldsymbol{\varphi}(\mathrm{X}, \mathrm{t})$ is then subjected to local conditions such that

$$\mathbf{F}^u := \partial_{\mathbf{X}} \boldsymbol{\varphi}(\mathbf{X}, t) \in \mathbb{R}^{n \otimes n}, \quad \text{and} \quad J^u := \det[\mathbf{F}^u] > 0,$$

where $\mathbf{F}^u$ is the displacement derived deformation gradient, whose jacobian is characterized as J^u. In the curvilinear setting, the displacement derived gradient can be expressed as a combination of covariant and contravariant basis vectors in the reference $(\mathbf{G}_i, \mathbf{G}^i)$ and current configurations $(\mathbf{g}_i, \mathbf{g}^i)$. With the usual notations, the metric tensors (general) in their basis vectors can be written as $\boldsymbol{\chi} = \chi_{ij} \boldsymbol{\chi}^i \otimes \boldsymbol{\chi}^j = \chi^{ij} \boldsymbol{\chi}_i \otimes \boldsymbol{\chi}_j$, see [74] for more details. Here, χ_{ij}, and χ^{ij} represents the covariant and contravariant components respectively. As a natural consequence of the curvilinear coordinates, Green-Lagrangian strain tensor $\mathbf{E}^u$ (derived via Cauchy-Green deformation) and the Second Piola-Kirchoff stress tensor $\mathbf{S}$ (PK2) in the reference configuration is estimated as

$$\mathbf{E}^u := \frac{1}{2} \left[g_{ij} - G_{ij} \right] \mathbf{G}^i \otimes \mathbf{G}^j; \qquad \mathbf{S} = S^{ij} \mathbf{G}_i \otimes \mathbf{G}_j. \tag{3}$$

4

Similarly, from the Stoke theorem, heat flux vector $\mathbf{Q}$ in the reference configuration takes the form

$$\mathbf{Q} = Q^i \mathbf{G}_i. \tag{4}$$

Complying with the solid shell approach, any position vector in the reference, $\mathbf{X}$, (and in the current configuration $\mathbf{x}$), can be expressed as a linear combination of the corresponding points on the top and bottom surface, (that are identified with the subscripts t and b, respectively) (see Fig. 1):

$$\mathbf{X}(\boldsymbol{\xi}) = \frac{1}{2}\left(1 + \xi^3\right)\mathbf{X}_t(\xi^1, \xi^2) + \frac{1}{2}\left(1 - \xi^3\right)\mathbf{X}_b(\xi^1, \xi^2), \tag{5}$$

$$\mathbf{x}(\boldsymbol{\xi}) = \frac{1}{2}\left(1 + \xi^3\right)\mathbf{x}_t(\xi^1, \xi^2) + \frac{1}{2}\left(1 - \xi^3\right)\mathbf{x}_b(\xi^1, \xi^2), \tag{6}$$

in the parametric space of natural coordinates $\mathcal{A} := \{\boldsymbol{\xi} = (\xi^1, \xi^2, \xi^3) \in \mathbb{R}^3 \mid -1 \leq \xi^i \leq +1; i = 1, 2, 3\}$. Here (ξ^1, ξ^2) represents in-plane directions and ξ^3 identifies thickness direction.

For the phase-field within the solid shell, as a consequence of the definition of position vectors, $\mathfrak{d}$ in the parametric space $\mathcal{A}$ is estimated as a linear combination of the top $(\mathfrak{d}_t)$ and bottom $(\mathfrak{d}_b)$ values expressed as

$$\mathfrak{d}(\boldsymbol{\xi}) = \frac{1}{2}\left(1 + \xi^3\right)\mathfrak{d}_t(\xi^1, \xi^2) + \frac{1}{2}\left(1 - \xi^3\right)\mathfrak{d}_b(\xi^1, \xi^2). \tag{7}$$

Using the previous derivations, the EAS method can be introduced to the total energy function. This is achieved by additive decomposition of the total Lagrangian strain $\mathbf{E}$ as a combination of displacement derived Green-Lagrangian strain $\mathbf{E}^u$ in Eq. (3) and incompatible strain $\tilde{\mathbf{E}}$. i,e $\mathbf{E} = \mathbf{E}^u + \tilde{\mathbf{E}}$. Consequently, the displacement derived deformation gradient ($\mathbf{F}$) is modified to accommodate the incompatible strain as $\mathbf{F} = \mathbf{F}^u + \tilde{\mathbf{F}}$ with corresponding modified jacobian takes the form $J = \det[\mathbf{F}] > 0$.

Based on these considerations, the total internal energy in Eq. (2) is modified to accommodate incompatible strain are expressed as

$$\Pi(\mathbf{u}, \tilde{\mathbf{E}}, \mathfrak{d}, T) = \int_{\mathcal{B}_0} g(\mathfrak{d})\Psi_0(\mathbf{E}^u, \tilde{\mathbf{E}}, T)\mathrm{d}\Omega + \int_{\mathcal{B}_0} \frac{\mathcal{G}_C}{4c_w}\left[\frac{\alpha(\mathfrak{d})}{l} + l\,|\nabla\mathfrak{d}|^2\right]\,\mathrm{d}\Omega + \Pi_{\mathrm{ext}}. \tag{8}$$

Here, $\Psi_0(\mathbf{E}^u, \tilde{\mathbf{E}}, T)$ is the intact free energy density function that involves the incompatible strains $\tilde{\mathbf{E}}$. Within this framework of Hu-Washizu variational principle, modified total internal energy takes the form

$$\Pi(\mathbf{u}, \tilde{\mathbf{E}}, \mathfrak{d}, T) = \int_{\mathcal{B}_0} g(\mathfrak{d})\Psi(\mathbf{u}, \tilde{\mathbf{E}}, T)\mathrm{d}\Omega - \int_{\mathcal{B}_0} \mathbf{S} : \tilde{\mathbf{E}}\,\mathrm{d}\Omega + \int_{\mathcal{B}_0} \frac{G_C}{4c_w}\left[\frac{\alpha(\mathfrak{d})}{l} + l\,|\nabla\mathfrak{d}|^2\right]\,\mathrm{d}\Omega + \Pi_{\mathrm{ext}}. \tag{9}$$

As described in the forthcoming section, it is worth noting that the ANS method is a collocation-based numerical technique, whose application is used for the treatment of the transverse shear and curvature thickness locking as proposed in [9, 93], see Fig. 1b).

For the intact free energy density function $\Psi(\mathbf{u}, \tilde{\mathbf{E}}, T)$, an isotropic Kirchoff-Saint-Venant material model is chosen, whose free energy in its local material forms reads

$$\Psi_0(\mathbf{E}, T) = \quad \frac{1}{2}\lambda\left(\mathrm{tr}[\mathbf{E}]\right)^2 + \mu\mathrm{tr}[\mathbf{E}^2] - 3\kappa\alpha\mathrm{tr}[\mathbf{E}]\left(T - T_0\right) \quad + c_p\left[\left(T - T_0\right) - T\log\frac{T}{T_0}\right], \tag{10}$$

where λ and μ are the Lamé constants, κ is the bulk modulus, and α is the coefficient of thermal expansion, whereas T_0 is the initial reference temperature. Moreover, Lamé constants and bulk modulus can be computed using Young's Modulus E and Poisson's ratio ν.

The constitutive equations can be now derived by complying conservation laws and second law of thermodynamics which in its local form leads to the Clausius-Duhem inequality, see [74] for more details.

5

2.3. Extension to FGMs

Within this context of functionally graded materials (FGMs), material properties changes across the domain. Let A and B be two materials compositions of a functionally graded materials, then the volume fraction (Vf_A) of the material A in the domain $\mathcal{B}_0$ can be defined as

$$Vf_A(\mathbf{x}) := Vf_A(\mathbf{x},\ \zeta,\ \boldsymbol{\mathcal{I}}) : \mathcal{B}_0 \to [0,1], \tag{11}$$

where ζ is the grading constant and $\boldsymbol{\mathcal{I}}$ is a set of internal variable that depends on the domain $\mathcal{B}_0$. Then, the volume fraction of the material B can be estimated as a function of material A, i.e., $Vf_B(\mathbf{x}) = 1 - Vf_A(\mathbf{x})$. Based on the rule of mixtures, the material properties such as Young's Modulus E, Poisson's ratio ν, coefficient of thermal expansion α, thermal conductivity k_0, heat capacity c_p and fracture energy $\mathcal{G}_C$ as a function of volume fraction of one of the material. Given $Vf_A(\mathbf{x})$ as a function with known values, the material properties take the form

$$E(\mathbf{x}) = E_A + (E_B - E_A)Vf_A(\mathbf{x}), \tag{12a}$$
$$\nu(\mathbf{x}) = \nu_A + (\nu_B - \nu_A)Vf_A(\mathbf{x}), \tag{12b}$$
$$\alpha(\mathbf{x}) = \alpha_A + (\alpha_B - \alpha_A)Vf_A(\mathbf{x}), \tag{12c}$$
$$k_0(\mathbf{x}) = k_{0,A} + (k_{0,B} - k_{0,A})Vf_A(\mathbf{x}), \tag{12d}$$
$$c_p(\mathbf{x}) = c_{p,A} + (c_{p,B} - c_{p,A})Vf_A(\mathbf{x}), \tag{12e}$$
$$\mathcal{G}_C(\mathbf{x}) = \mathcal{G}_{C,A} + (\mathcal{G}_{C,B} - \mathcal{G}_{C,A})Vf_A(\mathbf{x}). \tag{12f}$$

It can be argued that internal length scale l_c of the phase field approach to fracture is largely considered as material parameters [94]. In particular, the length scale l_c can be estimated using the relation $l_c = \dfrac{27}{256}\dfrac{\mathcal{G}_C E}{\sigma_c^2}$ for σ_c being apparent tensile strength, [48]. In order to include the vast literature regarding the choice of the length scale l_c, here the length scale is considered as a function of volume fraction i.e.,

$$l_c(\mathbf{x}) = l_{c,A} + (l_{c,B} - l_{c,A})Vf_A(\mathbf{x}). \tag{13}$$

But the special case of a spatially constant l_c can be achieved by setting $l_{c,A} = l_{c,B}$ for the two material phases A and B. Since Clausius-Duhem Inequality and the balance equations are defined locally, the Kirchoff-Saint-Venant in Eq. (10) is modified to accommodate FGMs as

$$\Psi_0(\mathbf{E}, T; \mathbf{X}) = \quad \tfrac{1}{2}\lambda(\mathbf{X})\left(\mathrm{tr}[\mathbf{E}]\right)^2 + \mu(\mathbf{X})\mathrm{tr}[\mathbf{E}^2] - 3\kappa(\mathbf{X})\alpha(\mathbf{X})\mathrm{tr}[\mathbf{E}]\left(T - T_0(\mathbf{X})\right)$$
$$+ c_p(\mathbf{X})\left[(T - T_0(\mathbf{X})) - T\log\tfrac{T}{T_0(\mathbf{X})}\right]. \tag{14}$$

Here, the material properties $\lambda(\mathbf{X})$, $\mu(\mathbf{X})$, $\kappa(\mathbf{X})$, $\alpha(\mathbf{X})$, $c_p(\mathbf{X})$, and $T_0(\mathbf{X})$ exhibit a variation in the spatial dimension. The material parameters from the surface energy, $\mathcal{G}_C$ and l, are also written as $\mathcal{G}_C(\mathbf{X})$ and $l(\mathbf{X})$ to explicitate such a spatial dependency. Moreover, the Lamé constants, $\kappa(\mathbf{X})$, $\mu(\mathbf{X})$ and the bulk modulus $\kappa(\mathbf{X})$ can be estimated as

$$\lambda(\mathbf{X}) = \frac{E(\mathbf{X})\nu(\mathbf{X})}{(1 + \nu(\mathbf{X}))(1 - 2\nu(\mathbf{X}))}; \qquad \mu(\mathbf{X}) = \frac{E(\mathbf{X})}{2(1 + \nu(\mathbf{X}))}; \qquad \kappa(\mathbf{X}) = \frac{\nu(\mathbf{X})E(\mathbf{X})}{3(\nu(\mathbf{X}) - 2)}, \qquad \text{for each } \mathbf{X} \in \mathcal{B}_0 \tag{15}$$

whereas $E(\mathbf{X})$ and $\nu(\mathbf{X})$ are computed according to Eqs. (12a) and (12b).

From the Clausius-Duhem inequality and the second law of thermodynamics, the equations corresponding to the second Piola-Kirchoff tensor $\mathbf{S}$ and entropy η read

$$\mathbf{S} := \partial_{\mathbf{E}}\Psi_0 = \lambda(\mathbf{X})\left(\mathrm{tr}[\mathbf{E}]\right)\mathbf{1} + 2\mu(\mathbf{X})\mathbf{E} - 3\kappa(\mathbf{X})\alpha(\mathbf{X})\left(T - T_0(\mathbf{X})\right)\mathbf{1}, \tag{16}$$

$$\eta := -\partial_T\Psi_0 = 3\kappa(\mathbf{X})\alpha(\mathbf{X})\mathrm{tr}[\mathbf{E}] + c_p(\mathbf{X})\log\frac{T}{T_0(\mathbf{X})}. \tag{17}$$

Note that, from here onward, the dependency on $\mathbf{X}$ is dropped from the material properties just to simplify the notation. The Clausius-Duhem inequality which ensures the thermodynamic consistency of the formulation takes the form

$$\mathcal{D}_{\mathrm{loc}} = [\mathbf{S} - \partial_{\mathbf{E}}\Psi] : \dot{\mathbf{E}} - [\eta + \partial_T\Psi]\dot{T} - \partial_{\nabla_{\mathbf{X}}T}\Psi : \nabla_{\mathbf{X}}\dot{T} - \partial_{\boldsymbol{\mathcal{I}}}\Psi : \dot{\boldsymbol{\mathcal{I}}} \geq 0, \tag{18}$$

where $\boldsymbol{\mathcal{I}}$ can be referred as a set of interval variables. Setting the damage variable $\mathfrak{d}$ as the internal variable among others, and putting Eqs. (16) and (17) into Eq. (18), leads to

$$\mathcal{D}_{\mathrm{loc}} := -\partial_{\boldsymbol{\mathcal{I}}}\Psi : \dot{\boldsymbol{\mathcal{I}}} = -\partial_{\mathfrak{d}}\Psi : \dot{\mathfrak{d}} \geq 0, \tag{19}$$

As a consequence of Eq. (19), we have that $\dot{\mathfrak{d}} \geq 0$ and $\partial_{\mathfrak{d}}\Psi = 0$ (or $\dot{\mathfrak{d}} = 0$ and $\partial_{\mathfrak{d}}\Psi \geq 0$) constituting irreversibility of the phase-field $\mathfrak{d}$ and the first order optimality condition for the evolution of phase-field, often referred as KKT conditions. The constitutive operators in the curvilinear setting reads

$$\mathbb{C} = \partial_{\mathbf{EE}}\Psi_0 = \left[\lambda G^{ij}G^{kl} + \mu\left(G^{ik}G^{jl} + G^{il}G^{jk}\right)\right]\mathbf{G}_i \otimes \mathbf{G}_j \otimes \mathbf{G}_k \otimes \mathbf{G}_l, \tag{20a}$$

$$\mathbf{Z} = \partial_{T\mathbf{E}}\Psi_0 = -3\kappa\alpha\left[G^{ij}\mathbf{G}_i \otimes \mathbf{G}_j\right], \tag{20b}$$

$$\mathbf{Q} = -J\mathbf{F}^{-1}\cdot\mathbf{k}\cdot\mathbf{F}^{-\mathrm{T}}\nabla_{\mathbf{X}}T. \tag{20c}$$

Here, $\mathbf{Z}$ and $\mathbf{Q}$ are second order tensor associated with free energy function and heat flux. The isotropic thermal conductivity $\mathbf{k}$ can be written using contravariant basis vectors as $\mathbf{k} = k(\mathbf{X})g^{ij}\mathbf{g}_i \otimes \mathbf{g}_i$.

With this, the solution of Eq. (2) can be obtained by solving the modified minimization problem

$$\boxed{\begin{array}{l}\text{Determine} \quad (\mathbf{u}, \tilde{\mathbf{E}}, \mathfrak{d}, T) \quad \text{from} \\ (\mathbf{u}^*, \tilde{\mathbf{E}}^*, \mathfrak{d}^*, T^*) = \arg\min_{\mathcal{S}}\Pi(\mathbf{u}, \tilde{\mathbf{E}}, \mathfrak{d}, T),\end{array}} \tag{21}$$

with $\mathcal{S} = \{\dot{\mathfrak{d}} \geq 0 \text{ for all } \mathbf{x} \in \mathcal{B}_0\}$. The set $(\mathbf{u}^*, \tilde{\mathbf{E}}^*, \mathfrak{d}^*, T^*)$ in Eq. (21) is solved by taking Gateaux derivative assuming enough regularity of the involved fields. For any admissible test function $(\delta\mathbf{u}, \delta\tilde{\mathbf{E}}, \delta\mathfrak{d}, \delta T)$ in $(\mathfrak{B}^u, \mathfrak{B}^{\tilde{E}}, \mathfrak{B}^{\mathfrak{d}}, \mathfrak{B}^T)$ in the appropriate space of distribution with

$$\mathfrak{B}^u = \{\delta\mathbf{u} \in \mathbf{H}^1(\mathcal{B}_0), \delta\mathbf{u} = 0 \text{ on } \partial\mathcal{B}_{0,\mathbf{u}}\}, \tag{22a}$$

$$\mathfrak{B}^{\tilde{E}} = \{\delta\tilde{E} \in \mathbf{L}^2(\mathcal{B}_0)\}, \tag{22b}$$

$$\mathfrak{B}^{\mathfrak{d}} = \{\delta\mathfrak{d} \in \mathbf{H}^1(\Omega)\big|\delta\mathfrak{d} \geq 0 \,\forall\, \mathbf{X} \in \mathcal{B}_0\}, \tag{22c}$$

$$\mathfrak{B}^T = \{\delta T \in \mathbf{H}^1(\Omega)\big|\delta T = 0 \text{ on } \partial\mathcal{B}_{0,q}\}, \tag{22d}$$

7

the following final multi-field problems is provided:

$$\mathcal{R}^u(\mathbf{u}, \tilde{\mathbf{E}}, \mathfrak{d}, T, \delta\mathbf{u}) = \int_{\mathcal{B}_0} g(\mathfrak{d}) \left[\mathbf{S} : \delta\mathbf{E}^u\right] \, \mathrm{d}\Omega - \int_{\mathcal{B}_0} \rho_0 \bar{\boldsymbol{\gamma}} \delta\mathbf{u} \, \mathrm{d}\Omega - \int_{\partial\mathcal{B}_{0,t}} \hat{\mathbf{t}} \delta\mathbf{u} \, \mathrm{d}\partial\Omega = 0,$$
$$\mathcal{R}^u = \mathcal{R}^u_{\mathrm{int}} - \mathcal{R}^u_{\mathrm{ext}} = 0,$$
(23a)

$$\mathcal{R}^{\tilde{E}}(\mathbf{u}, \tilde{\mathbf{E}}, \mathfrak{d}, T, \delta\tilde{\mathbf{E}}) = \int_{\mathcal{B}_0} g(\mathfrak{d}) \left[\mathbf{S} : \delta\tilde{\mathbf{E}}\right] \, \mathrm{d}\Omega = \mathcal{R}^{\tilde{E}}_{\mathrm{int}} = 0,$$
(23b)

$$\mathcal{R}^{\mathfrak{d}}(\mathbf{u}, \tilde{\mathbf{E}}, \mathfrak{d}, T, \delta\mathfrak{d}) = \int_{\mathcal{B}_0} \mathcal{G}_C \left[\frac{\mathfrak{d}}{l}\delta\mathfrak{d} + l\nabla\mathfrak{d} \cdot \nabla\delta\mathfrak{d}\right] \, \mathrm{d}\Omega - \int_{\mathcal{B}_0} 2(1-\mathfrak{d})\Psi(\mathbf{u}, \tilde{\mathbf{E}}, T)\delta\mathfrak{d} \, \mathrm{d}\Omega = 0,$$
(23c)

$$\mathcal{R}^T(\mathbf{u}, \tilde{\mathbf{E}}, \mathfrak{d}, T, \delta T) = \int_{\mathcal{B}_0} c_p \dot{T} \delta T \, \mathrm{d}\Omega - \int_{\mathcal{B}_0} g(\mathfrak{d}) \left[T\mathbf{Z} : \dot{\mathbf{E}}\right] \delta T \, \mathrm{d}\Omega$$
$$+ \int_{\partial\mathcal{B}_{0,q}} Q_N \delta T \, \mathrm{d}\partial\Omega + \int_{\mathcal{B}_0} g(\mathfrak{d}) Jk \left[\nabla_{\mathbf{X}} \delta T\right]^{\mathrm{T}} \mathbf{C}^{-1} \nabla_{\mathbf{X}}[T] \, \mathrm{d}\Omega = 0.$$
(23d)

3. Finite Element Implementation

Following the standard isoparametric interpolation arguments, the functional space $\mathcal{B}_0$ is discretized such that $\mathcal{B}_0 \approx \bigcup_{e=1}^{n_e} \mathcal{B}_0^{(e)}$ for n_e non-overlapping elements. The discrete reference and current position vectors are interpolated via standard trilinear shape function N^I ($\mathbf{N}(\boldsymbol{\xi})$ in matrix notation) as

$$\mathbf{X} \approx \sum_{I=1}^{8} N^I(\boldsymbol{\xi})\mathbf{X}_I = \mathbf{N}(\boldsymbol{\xi})\widetilde{\mathbf{X}} \quad \text{and} \quad \mathbf{x} \approx \sum_{I=1}^{8} N^I(\boldsymbol{\xi})\mathbf{x}_I = \mathbf{N}(\boldsymbol{\xi})\widetilde{\mathbf{x}},$$
(24)

for the respective global vectors $\widetilde{\mathbf{X}}$ and $\widetilde{\mathbf{x}}$.

The interpolation of the fields $(\mathbf{u}, \tilde{\mathbf{E}}, \mathfrak{d}, T)$, their respective variations $(\delta\mathbf{u}, \delta\tilde{\mathbf{E}}, \delta\mathfrak{d}, \delta T)$ takes the form

$$\mathbf{u} \approx \mathbf{N}(\boldsymbol{\xi})\mathbf{d}; \quad \tilde{\mathbf{E}} \approx \mathbf{M}(\boldsymbol{\xi})\boldsymbol{\varsigma}; \quad \mathfrak{d} \approx \mathbf{N}(\boldsymbol{\xi})\tilde{\mathfrak{d}}; \quad T \approx \hat{\mathbf{N}}(\boldsymbol{\xi})\hat{T},$$
(25a)

$$\delta\mathbf{u} \approx \mathbf{N}(\boldsymbol{\xi})\delta\mathbf{d}; \quad \delta\tilde{\mathbf{E}} \approx \mathbf{M}(\boldsymbol{\xi})\delta\boldsymbol{\varsigma}; \quad \delta\mathfrak{d} \approx \mathbf{N}(\boldsymbol{\xi})\delta\tilde{\mathfrak{d}}; \quad \delta T \approx \hat{\mathbf{N}}(\boldsymbol{\xi})\delta\hat{T}.$$
(25b)

Here, the $\boldsymbol{\varsigma}$ is the collection of EAS parameters and $\mathbf{M}(\boldsymbol{\xi})$ is the enhancing interpolation matrix. In particular, the operator $\mathbf{M}(\boldsymbol{\xi})$ is equipped with 7 parameters at each element suitable to alleviate volumetric, membrane and Poisson's thickness locking. Within the natural co-ordinate system $\boldsymbol{\xi} = \{\xi^1, \xi^2, \xi^3\}$, the operator $\mathbf{M}(\boldsymbol{\xi})$ takes the form

$$\mathbf{M} = \begin{bmatrix} \xi^1 & 0 & 0 & 0 & 0 & 0 & 0 \\ 0 & \xi^1 & 0 & 0 & 0 & 0 & 0 \\ 0 & 0 & \xi^3 & \xi^1\xi^3 & \xi^2\xi^3 & 0 & 0 \\ 0 & 0 & 0 & 0 & 0 & \xi^1 & \xi^2 \\ 0 & 0 & 0 & 0 & 0 & 0 & 0 \\ 0 & 0 & 0 & 0 & 0 & 0 & 0 \end{bmatrix}.$$
(26)

8

Note that, it is also possible to have 11 parameters at each elemental level as in [74], but 7 parameters are chosen here for the sake of reducing complexity of the model.

In order to circumvent transverse shear and trapezoidal locking, the transverse shear (E_{13}, E_{23}) and transverse normal strain (E_{33}) are modified according to ANS interpolation method. The interpolation of the transverse shear strains and transverse normal strains are performed at points (A, B, C, D) and (O, P, S, T) respectively as in Fig. 1. Accordingly, the modified strains takes the form

$$\begin{Bmatrix} 2E_{13}^{ANS} \\ 2E_{23}^{ANS} \end{Bmatrix} = \begin{Bmatrix} (1 - \xi^2)2E_{13}(\boldsymbol{\xi}_A) + (1 + \xi^2)2E_{13}(\boldsymbol{\xi}_C) \\ (1 + \xi^1)2E_{23}(\boldsymbol{\xi}_B) + (1 - \xi^1)2E_{23}(\boldsymbol{\xi}_D) \end{Bmatrix}. \tag{27}$$

and

$$E_{33}^{ANS} = \sum_{m=O,P,S,T} N^m(\xi^1, \xi^2)E_{33};$$

$$N^m(\xi^1, \xi^2) = \frac{1}{4} \left(1 + \xi_m^1 \xi^1\right) \left(1 + \xi_m^2 \xi^2\right), \tag{28}$$

$$\text{with } \xi_m^1, \xi_m^2 = \pm 1.$$

The displacement derived compatible strain tensor $\mathbf{E}^u$ are interpolated using displacement strain operator $\mathbf{B}$ as

$$\mathbf{E}^u \approx \mathbf{B}(\mathbf{d})\mathbf{d}, \quad \delta\mathbf{E}^u \approx \mathbf{B}(\mathbf{d})\delta\mathbf{d}, \tag{29}$$

Similarly, gradient of the phase-field $\nabla_{\mathbf{x}}\mathfrak{d}$ and gradient of temperature $\nabla_{\mathbf{X}}T$ are interpolated as

$$\nabla_{\mathbf{x}}\mathfrak{d} \approx \mathbf{B}^{\mathfrak{d}}(\mathbf{d})\tilde{\mathfrak{d}}, \quad \nabla_{\mathbf{x}}\delta\mathfrak{d} \approx \mathbf{B}^{\mathfrak{d}}(\mathbf{d})\delta\tilde{\mathfrak{d}}, \tag{30a}$$

$$\nabla_{\mathbf{X}}T = \mathbf{G}^{-1}\nabla_{\boldsymbol{\xi}}T \approx \mathbf{G}^{-1}\nabla_{\boldsymbol{\xi}}\hat{\mathbf{N}}(\boldsymbol{\xi})\hat{\boldsymbol{T}}; \quad \nabla_{\mathbf{X}}\delta T \approx \mathbf{G}^{-1}\nabla_{\boldsymbol{\xi}}\hat{\mathbf{N}}(\boldsymbol{\xi})\delta\hat{\boldsymbol{T}}; \tag{30b}$$

where $\mathbf{B}^{\mathfrak{d}}$ is suitable gradient operator and $\nabla_{\boldsymbol{\xi}}$ is the gradient of temperature with respect to natural coordinates in curvilinear setting.

For each pseudo-time step increment $\Delta t := t_{n+1}^{(k)} - t_n > 0$, assuming that the fields $(\mathbf{u}, \tilde{\mathbf{E}}, \mathfrak{d}, T)_{t_n}$ at time step t_n is known, the unknown fields $(\mathbf{u}, \tilde{\mathbf{E}}, \mathfrak{d}, T)_{t_{n+1}}$ are computed via consistent linearization of the residual functions. Following the standard finite element procedure, Eqs. (23a), (23b), (23c), (23d), can be expressed as a system of linear equations

$$\begin{bmatrix} \mathbf{K_{dd}} & \mathbf{K_{d\varsigma}} & \mathbf{K_{d\tilde{\mathfrak{d}}}} & \mathbf{K}_{dT} \\ \mathbf{K_{\varsigma d}} & \mathbf{K_{\varsigma\varsigma}} & \mathbf{K_{\varsigma\tilde{\mathfrak{d}}}} & \mathbf{K}_{\varsigma T} \\ \mathbf{K_{\tilde{\mathfrak{d}}d}} & \mathbf{K_{\tilde{\mathfrak{d}}\varsigma}} & \mathbf{K_{\tilde{\mathfrak{d}}\tilde{\mathfrak{d}}}} & \mathbf{K}_{\tilde{\mathfrak{d}}T} \\ \mathbf{K}_{Td} & \mathbf{K}_{T\varsigma} & \mathbf{K}_{T\tilde{\mathfrak{d}}} & \mathbf{K}_{TT} \end{bmatrix} \begin{bmatrix} \Delta\mathbf{d} \\ \Delta\boldsymbol{\varsigma} \\ \Delta\mathfrak{d} \\ \Delta\hat{\boldsymbol{T}} \end{bmatrix} = \begin{bmatrix} \hat{\mathcal{R}}_{\text{ext}}^u \\ \mathbf{0} \\ \mathbf{0} \\ \hat{\mathcal{R}}_{\text{ext}}^T \end{bmatrix} - \begin{bmatrix} \hat{\mathcal{R}}_{\text{int}}^u \\ \hat{\mathcal{R}}_{\text{int}}^{\varsigma} \\ \hat{\mathcal{R}}_{\text{int}}^{\tilde{\mathfrak{d}}} \\ \hat{\mathcal{R}}_{\text{int}}^T \end{bmatrix}. \tag{31}$$

The different elements of tangent stiffness matrix reads

$$\mathbf{K_{dd}} = \int_{\mathcal{B}_0} g(\mathfrak{d}) \left(\mathbf{B}(\mathbf{d})^{\text{T}}\mathbb{C}\mathbf{B}(\mathbf{d}) + \left[\frac{\partial\mathbf{B}(\mathbf{d})}{\partial\mathbf{d}}\right]^{\text{T}} \mathbf{S} \right) \, \mathrm{d}\Omega = \mathbf{K}_{\mathbf{dd},\text{mat}} + \mathbf{K}_{\mathbf{dd},\text{geom}}$$

$$\mathbf{K_{d\varsigma}} = \int_{\mathcal{B}_0} g(\mathfrak{d})\mathbf{M}(\boldsymbol{\xi})^{\text{T}}\mathbb{C}\mathbf{B}(\mathbf{d}) \, \mathrm{d}\Omega; \quad \mathbf{K_{d\tilde{\mathfrak{d}}}} = \int_{\mathcal{B}_0} -2(1 - \mathfrak{d})\mathbf{B}(\mathbf{d})^{\text{T}}\mathbf{SN}(\boldsymbol{\xi}) \, \mathrm{d}\Omega, \tag{32a}$$

$$\mathbf{K}_{dT} = \int_{\mathcal{B}_0} g(\mathfrak{d})\mathbf{B}(\mathbf{d})^{\text{T}}\mathbf{Z}\hat{\mathbf{N}}(\boldsymbol{\xi}) \, \mathrm{d}\Omega,$$

9

$$\mathbf{K}_{\varsigma u} = \int_{\mathcal{B}_0} g(\mathfrak{d})\mathbf{M}(\boldsymbol{\xi})^{\mathrm{T}}\mathbb{C}\mathbf{B}(\mathbf{d})\ \mathrm{d}\Omega; \qquad \mathbf{K}_{\varsigma\varsigma} = \int_{\mathcal{B}_0} g(\mathfrak{d})\mathbf{M}(\boldsymbol{\xi})^{\mathrm{T}}\mathbb{C}\mathbf{M}(\boldsymbol{\xi})\ \mathrm{d}\Omega,$$

$$\mathbf{K}_{\varsigma\tilde{\mathfrak{d}}} = \int_{\mathcal{B}_0} -2(1-\mathfrak{d})\mathbf{M}(\boldsymbol{\xi})^{\mathrm{T}}\mathbf{S}\mathbf{N}(\boldsymbol{\xi})\ \mathrm{d}\Omega; \qquad \mathbf{K}_{\varsigma T} = \int_{\mathcal{B}_0} \mathbf{M}(\boldsymbol{\xi})^{\mathrm{T}}\mathbf{Z}\hat{\mathbf{N}}(\boldsymbol{\xi})\ \mathrm{d}\Omega, \tag{32b}$$

$$\mathbf{K}_{\tilde{\mathfrak{d}}\mathbf{d}} = \int_{\mathcal{B}_0} -2(1-\mathfrak{d})\mathbf{N}(\boldsymbol{\xi})^{\mathrm{T}}\mathbf{S}\mathbf{B}(\mathbf{d})\ \mathrm{d}\Omega; \qquad \mathbf{K}_{\tilde{\mathfrak{d}}\varsigma} = \int_{\mathcal{B}_0} -2(1-\mathfrak{d})\mathbf{N}(\boldsymbol{\xi})^{\mathrm{T}}\mathbf{S}\mathbf{M}(\boldsymbol{\xi})\ \mathrm{d}\Omega,$$

$$\mathbf{K}_{\tilde{\mathfrak{d}}\tilde{\mathfrak{d}}} = \int_{\mathcal{B}_0} \left[2\frac{\mathcal{G}_C}{l}\mathcal{H}\right]\mathbf{N}(\boldsymbol{\xi})^{\mathrm{T}}\mathbf{N}(\boldsymbol{\xi})\ \mathrm{d}\Omega + \int_{\mathcal{B}_0} 2\mathcal{G}_C l\mathbf{B}^{\mathfrak{d}}(\boldsymbol{\xi})^{\mathrm{T}}\mathbf{B}^{\mathfrak{d}}(\boldsymbol{\xi})\ \mathrm{d}\Omega, \tag{32c}$$

$$\mathbf{K}_{\tilde{\mathfrak{d}}T} = \int_{\mathcal{B}_0} -2(1-\mathfrak{d})\mathbf{N}(\boldsymbol{\xi})\mathbf{B}^T(\mathbf{d})\hat{\mathbf{N}}(\boldsymbol{\xi})\ \mathrm{d}\Omega,$$

$$\mathbf{K}_{T\mathbf{d}} = \int_{\mathcal{B}_0} g(\mathfrak{d})\Delta_{\mathbf{d}}[J]\mathbf{B}_T^{\mathrm{T}}\mathbf{F}^{-1}\cdot\mathbf{k}\cdot\mathbf{F}^{-\mathrm{T}}\nabla_{\mathbf{X}}T\ \mathrm{d}\Omega,$$

$$+ \int_{\mathcal{B}_0} g(\mathfrak{d})J\mathbf{B}_T^{\mathrm{T}}\left(\Delta_{\mathbf{d}}[\mathbf{F}^{-1}]\cdot\mathbf{k}\cdot\mathbf{F}^{-\mathrm{T}} + \mathbf{F}^{-1}\cdot\mathbf{k}\cdot\Delta_{\mathbf{d}}[\mathbf{F}^{-\mathrm{T}}]\right)\nabla_{\mathbf{X}}T\ \mathrm{d}\Omega - \int_{\mathcal{B}_0}\hat{\mathbf{N}}^{\mathrm{T}}\frac{T}{\Delta t}\mathbf{Z}^{\mathrm{T}}\mathbf{B}\ \mathrm{d}\Omega,$$

$$\mathbf{K}_{T\varsigma} = -\int_{\mathcal{B}_0}\hat{\mathbf{N}}(\boldsymbol{\xi})^{\mathrm{T}}\frac{T}{\Delta t}\mathbf{Z}^{\mathrm{T}}\mathbf{M}(\boldsymbol{\xi})\ \mathrm{d}\Omega; \quad \mathbf{K}_{T\mathfrak{d}} = -\int_{\mathcal{B}_0} -2(1-\mathfrak{d})\hat{\mathbf{N}}(\boldsymbol{\xi})^{\mathrm{T}}(\mathbf{Z}^{\mathrm{T}}\dot{\mathbf{E}})\mathbf{N}(\boldsymbol{\xi})\ \mathrm{d}\Omega, \tag{32d}$$

$$\mathbf{K}_{TT} = \int_{\mathcal{B}_0}\hat{\mathbf{N}}(\boldsymbol{\xi})^{\mathrm{T}}\frac{c_p}{\Delta t}\hat{\mathbf{N}}(\boldsymbol{\xi})\ \mathrm{d}\Omega - \int_{\mathcal{B}_0} g(\mathfrak{d})\hat{\mathbf{N}}(\boldsymbol{\xi})^{\mathrm{T}}(\mathbf{Z}^{\mathrm{T}}\dot{\mathbf{E}})\hat{\mathbf{N}}(\boldsymbol{\xi})\ \mathrm{d}\Omega + \int_{\mathcal{B}_0} g(\mathfrak{d})J\mathbf{B}_T^{\mathrm{T}}\mathbf{F}^{-1}\cdot\mathbf{k}\cdot\mathbf{F}^{-\mathrm{T}}\mathbf{B}_T\ \mathrm{d}\Omega.$$

with $\mathcal{H}$ being the crack driving force (history variable) as in [93] takes the form

$$\mathcal{H} = \max_{\tau\in[0,t]}\left[\Psi(\mathbf{u}, \tilde{\mathbf{E}}, T)\right], \tag{33}$$

Here, $\mathbf{k}_{\mathbf{dd},\mathrm{geom}}$ and $\mathbf{k}_{\mathbf{dd},\mathrm{mat}}$ refers to the geometric and material contributions, whereas $\Delta_{\mathbf{d}}[J]$, $\Delta_{\mathbf{d}}[\mathbf{F}^{-1}]$ and $\Delta_{\mathbf{d}}[\mathbf{F}^{-\mathrm{T}}]$ are the consistent linearization of the Jacobian J of the transformation $\mathbf{F}$, the inverse of the displacement-derived deformation gradient and its transpose, respectively with respect to the kinematic field, see [74] for computation of these terms.

Owing to inter element continuity of enhanced strains, the above stiffness matrix can be condensed at element level via a standard condensation process as

$$\begin{bmatrix}\mathbf{K}_{\mathbf{dd}}^* & \mathbf{K}_{\mathbf{d}\tilde{\mathfrak{d}}}^* & \mathbf{K}_{\mathbf{d}T}^* \\ \mathbf{K}_{\tilde{\mathfrak{d}}\mathbf{d}}^* & \mathbf{K}_{\tilde{\mathfrak{d}}\tilde{\mathfrak{d}}}^* & \mathbf{K}_{\tilde{\mathfrak{d}}T}^* \\ \mathbf{K}_{T\mathbf{d}}^* & \mathbf{K}_{T\tilde{\mathfrak{d}}}^* & \mathbf{K}_{TT}^*\end{bmatrix}\begin{bmatrix}\Delta\mathbf{d} \\ \Delta\mathfrak{d} \\ \Delta\hat{\boldsymbol{T}}\end{bmatrix} = \begin{bmatrix}\tilde{\tilde{\mathcal{R}}}^{\mathbf{d}} \\ \tilde{\tilde{\mathcal{R}}}^{\mathfrak{d}} \\ \tilde{\tilde{\mathcal{R}}}^{T}\end{bmatrix} \tag{34}$$

where $\mathbf{K}_{ij}^* = \mathbf{K}_{ij} - \mathbf{K}_{i\varsigma}\mathbf{K}_{\varsigma\varsigma}^{-1}\mathbf{K}_{\varsigma j}$ and $\tilde{\tilde{\mathcal{R}}}^j = \mathcal{R}_{ext}^j - \mathcal{R}_{int}^j + \mathbf{K}_{i\varsigma}\mathbf{K}_{\varsigma\varsigma}^{-1}\mathcal{R}_{int}^{\varepsilon}$ for each $i,j = \{\mathbf{d}, \mathfrak{d}, T\}$.

Owing to the staggered scheme implementation, the coupled terms $\mathbf{K}_{d\varsigma}, \mathbf{K}_{dT}, \mathbf{K}_{T\varsigma}, \mathbf{K}_{T\mathfrak{d}}, \mathbf{K}_{\tilde{\mathfrak{d}}T}, \mathbf{K}_{\tilde{\mathfrak{d}}\varsigma}\mathbf{K}_{\varsigma T} = 0$ for implementation. The resulting system of algebraic system in Eq. (34) can be solved using the Newton-Raphson solver or the Broyden-Fletcher-Goldfarb-Shanna (BFGS) solver. In the following numerical application, plate with multiple holes and cylinder with grading are solved using Newton solver, whereas all the others are solved using BFGS solver. Note that for the problem involving geometric non-linearity (i.e cylinder with grading and plate with multiple holes), BFGS solver computation times increases significantly leading to increased iteration required for convergence at each step, hence, Newton solver is used. For problem without geometric non-linearity, BFGS shows efficient computation. The comparison between the solvers in terms of CPU time or iteration is out of scope for the current article. See [95–97] for details regarding the BFGS solver.

Material	E (MPa)	ν	$\alpha(10^{-6}/^oK)$	$k_0(W/mm^oK)$	$c_p(kJ/kg^oK)$	$\mathcal{G}_C$ (MPa$\sqrt{mm}$)	l_c (mm)
Copper	120×10^3	0.34	16.5	150	0.372	11.968	0.1
Titanium	116×10^3	0.34	8.90	17	0.72	5.9973	0.1267
Zirconia	210×10^3	0.31	10.1	5.05	0.4	0.32	0.06
Alumina	380×10^3	0.26	7.7	25	0.880	0.06634	0.08
Silicon carbide	410×10^3	0.35	4	120	0.750	0.045643	0.003
Polymer Glass	85×10^3	0.21	5.1	1.35	0.805	0.007197	0.008

Table 1: Properties of the simulated materials.
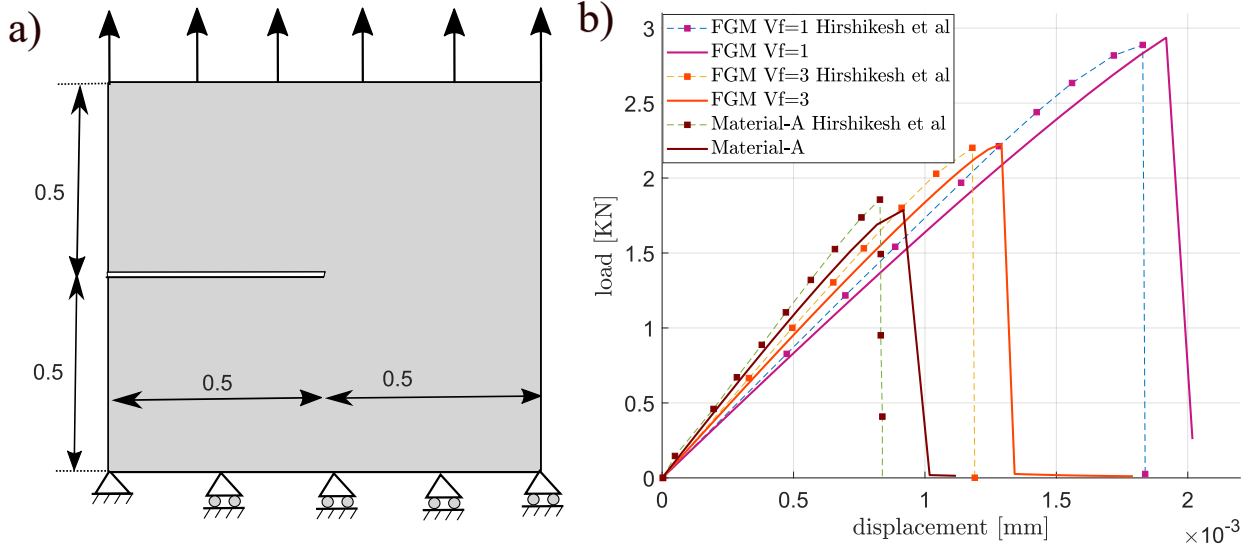
Figure 2: (a) Geometric description of the model, (b) force vs. displacement plots comparison with Hrishikesh et al [49].

4. Numerical applications

In this section, the predictive capability of the proposed thermo-mechanical solid shell formulation with phase-field for functionally graded materials is assessed using several representative examples. First, a benchmark test is proposed. Then, the numerical aspects concerning the grading are discussed by introducing a volume fraction that can describe the change of material properties. The examples of a plate with two notches and a plate with many holes are examined to study the deflection of cracks due to material properties grading and temperature effects. Later, a thin cylindrical shell is analyzed to show the applicability of the proposed model to complex structures. The classic benchmark examples concerning a plate with a notch is considered to study the effects of Young's modulus on crack propagation and temperature distribution using metal-metal, ceramic-polymer, and ceramic-ceramic FGM specimens. A three-phase FGM is finally considered to pinpoint the influence grading on the material behavior.

The details on the function Vf_A and the discussion on grading are provided for each example for more clarity. In order to show examples spanning the wide range of material behavior, six material parameters are considered spanning metals, ceramic, and polymers, namely: Copper (metal), Titanium (metal), Alumina (ceramic), Zirconia (ceramic), Silicon carbide (ceramic) and polymer glass (polymer) whose material properties are given in Tab. 1.

4.1. Verification example

This example concerns the verification of the proposed model. Due to the scarce experiment concerning

11
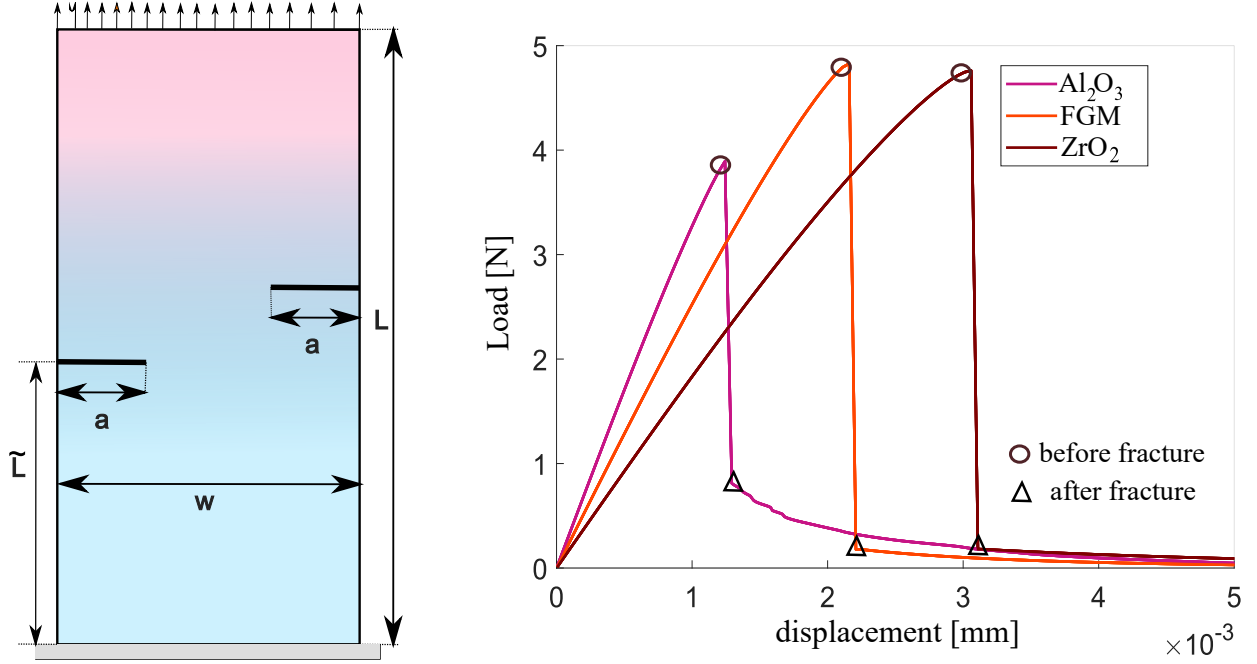
Figure 3: (left) Geometric description of the model, (right) force vs. displacement plots with $\zeta = 1$ in Eq. (36) and its homogeneous components.

thermo-mechanical FGMs, the numerical results has been compared against elastic numerics in two dimension [49]. Equal temperature is applied everywhere throughout the analysis to eliminate the temperature effects. Fig. 2a) shows the sketch of the model under consideration with grading in $y-$direction such that alumina (material-A) occupies the top surface, and zirconia (material-B) occupies the bottom surface. The material properties of alumina and zirconia are shown in Tab. 1. The volume fraction function is defined as

$$V f_A = \left(\frac{y}{1}\right)^{\zeta} \quad \text{for} \quad 0 \leq y \leq L. \tag{35}$$

The force vs. displacement curve for homogeneous material (material-A) and the FGM with $\zeta = 1$, and $\zeta = 3$ with $l = 0.006$ are compared against the experiments in [49] as in Fig. 2b). A satisfactory agreement between the two can be observed. The small discrepancy in the results maybe stemming from the fact that numerical experiments in [49] are done in plane strain conditions, whereas the developed model in this article considers three-dimensional constitutive law.

4.2. Plate with two edge notches

This example concerns the application of the proposed model to functionally graded double edged asymmetrical notched specimen comprising Alumina (Al$_2$O$_3$) and Zirconia (ZrO$_2$) with grading in $y-$direction, with alumina on the top and zirconia on the bottom. Fig. 3 shows the sketch of the model under consideration with $L = 2$ mm, $a = 0.3$ mm, $w = 1$ mm, $\tilde{L} = 0.9$ mm, and thickness $h = 0.028$ mm. The model is discritized with 4896 elements. The bottom of the specimen is fully restrained whereas the displacement of $\Delta = 0.005$ mm is applied on the top edge. The properties of alumina and zirconia are shown in Tab. 1. With alumina being considered as material-A, the volume fraction function is defined as

$$V f_A = \left(\frac{y}{2}\right)^{\zeta} \quad \text{for} \quad 0 \leq y \leq L. \tag{36}$$

12
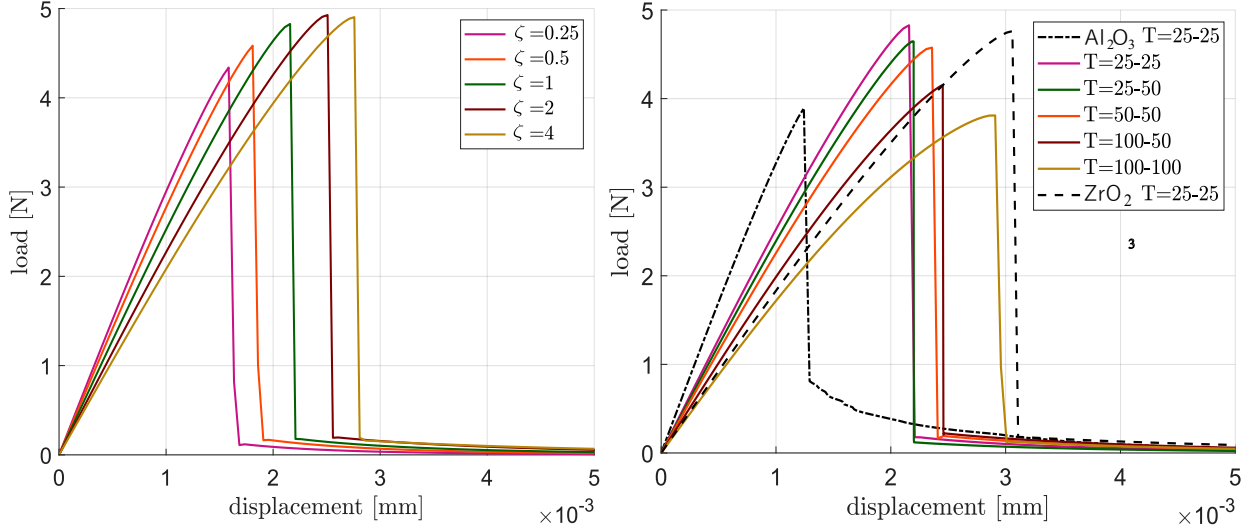
Figure 4: Force vs displacement curve for (left) variation of grading function ζ and (right) variation of temperature boundary conditions for double notched plate.

The evolution force vs. displacement curves of the homogeneous materials and of the FGM with $\zeta = 1$ (linear) are shown in Fig. 3. In these examples, a temperature of $T_1 = T_2 = 25^o$C is applied on the left and right edges, respectively. Due to the thermo-elastic mismatch, the maximum load-bearing capacity and the thermal distributions are different in FGM compared to its homogeneous constituents.

Since the thermal conductivity of the alumina is five times larger than zirconia, the temperature distribution in FGM is unequal, and high temperatures are largely concentrated towards the top surface (alumina). The difference in temperature distributions between the homogeneous material (alumina) and the FGM are shown in Fig. 5 along with the crack propagation at different time instances. Notice that from Eq. (32d), the degradation function $g(\mathfrak{d})$ is applied on the $\mathbf{Z}$ and $\boldsymbol{Q}$ matrix which contains the thermal conductivity $\mathbf{k}$. As the $\mathfrak{d}$ approaches 1, $\mathbf{k}$ tends to 0. In the region of crack propagation, $\mathbf{k}$ is almost zero and acts as a thermal barrier which can be observed in Fig. 5. Moreover, Fig. 4(Right) shows the force vs. displacement curve for the variation of temperature boundary condition with $\zeta = 1$. It can be noticed that, as the temperature increases, the load-bearing capacity decreases.

Referring to the other material properties' mismatch, the Young's modulus E and the fracture energy $\mathcal{G}_C$, and subsequently the characteristic length scale l_c, they play a vital role in determining the load-bearing capacity. It can be observed from Fig. 3 that, as expected, the initial slope depends on Young's modulus, whereas the peak response (load-bearing capacity) depends on the $\mathcal{G}_C$ and l_c (that are related to the apparent strength). Due to the fact that the alumina has the highest value of E and the lowest value of $\mathcal{G}_C$ among the two materials herein considered, the slope of alumina is higher, and the maximum load-bearing capacity is lower than zirconia. Since the properties of FGM are a linear/nonlinear combination of its homogeneous materials, the crack deflection of the FGM is different compared to the homogeneous materials as shown in Fig. 5. Moreover, Fig. 4 (left panel) shows the evolution of force vs. displacement curve for the variation of grading parameter ζ with the same temperature boundary condition as before. Naturally, as ζ goes to infinity, the load-bearing capacity approaches that of zirconia.

For the pure elastic analysis (without temperature imposed), the maximum load-bearing capacity of the FGM is always bounded between its homogeneous constituents, see [48] for more details. When the temperature effects are considered, this is partially true. For the same boundary temperatures, the maximum load-bearing capacity of the FGM is bounded between its homogeneous constitutes, whose mathematical proof is a simple extension of Theorem- 3 in [48]. In contrast, the peak load cannot be predicted accurately based on the energy bounds when different boundary temperatures are applied between FGM and its
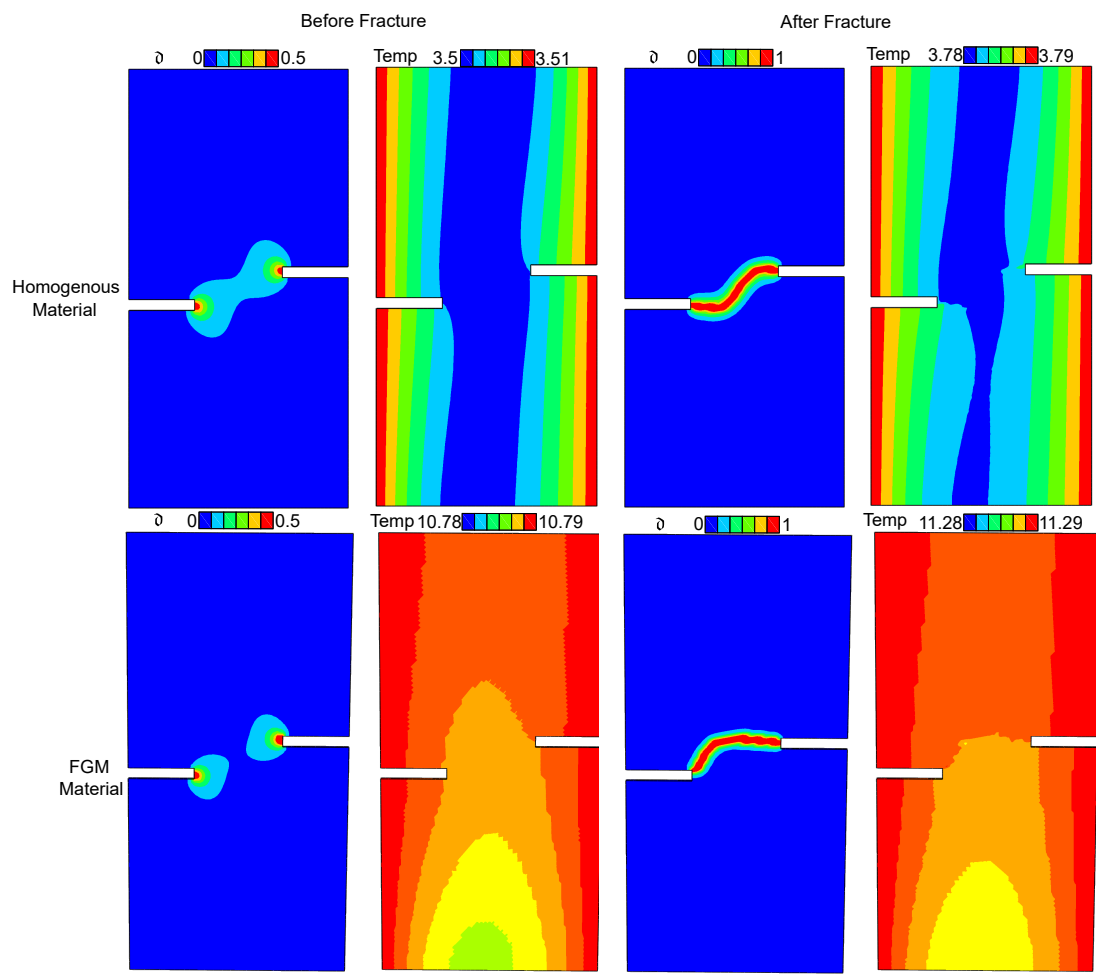
Figure 5: Double edge notched plate: phase-field and temperature distribution during initiation of fracture, and at failure.
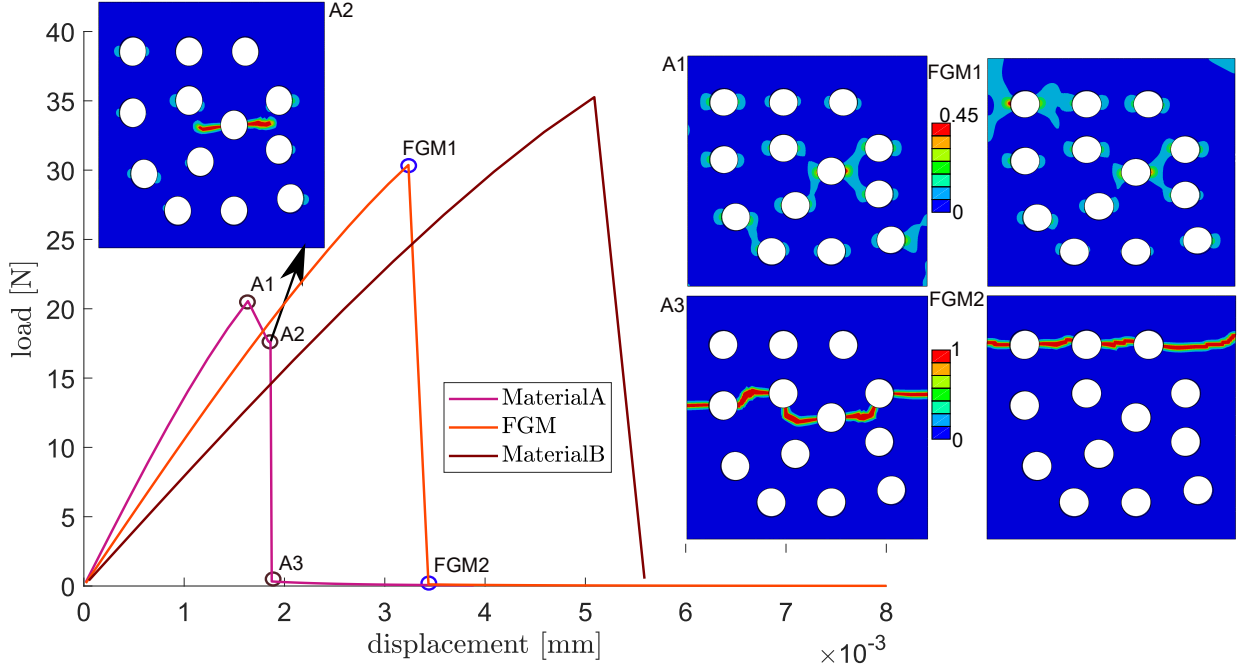
Figure 6: Plate with holes: force vs. displacement curves and the differences in crack propagation between FGM and homogeneous case.

homogeneous materials.

4.3. Plate with multiple holes

In this example, the proposed model investigates crack deflection in FGMs. For this, a square plate of length $L = 2.5$ mm and thickness $h = 0.056$ mm is considered. The square plate contains 12 holes of radius $r = 0.125$ mm randomly placed across the plate. The model is discritized with 11209 elements. Similar to the previous example, the plate consists of FGM made up of alumina-zirconia graded in $y-$direction. In this example, a constant length scale $l_c = 0.06$ mm is considered for both homogeneous and FGM. See also [49]. The bottom surface made of zirconia (material-B) is restrained, and a vertical displacement is applied on the top surface made of alumina (material-A). The temperature of $25^o C$ is applied on both lateral sides. The volume fraction is defined as

$$Vf_A = \left(\frac{y}{2.5}\right)^\zeta \quad 0 \leq y \leq L; \qquad \implies Vf_B = (1 - Vf_A). \tag{37}$$

Fig. 6 shows the evolution of force vs. displacement curve for the FGM with $\zeta = 1$ and is compared to its homogeneous constituents. Owing to the lower fracture of alumina, it can be seen that the crack initiation and propagation in FGM occur near the top surface compared to the central crack in the homogeneous surrogate.

The temperature distribution is very similar to the previous example where the temperature is concentrated towards the top surface. Recalling the reduction of thermal conductance due to crack propagation, the thermal insulation of the crack path can be observed in Fig. 7.

4.4. Cylinder with grading

In this example, a curved cylinder of radius $R = 2$ mm and length $L = 20$ mm with a central hole of radius $r = 0.15$ mm is made of FGM (alumina-zirconia) is considered. The model is discritized with 12491

15
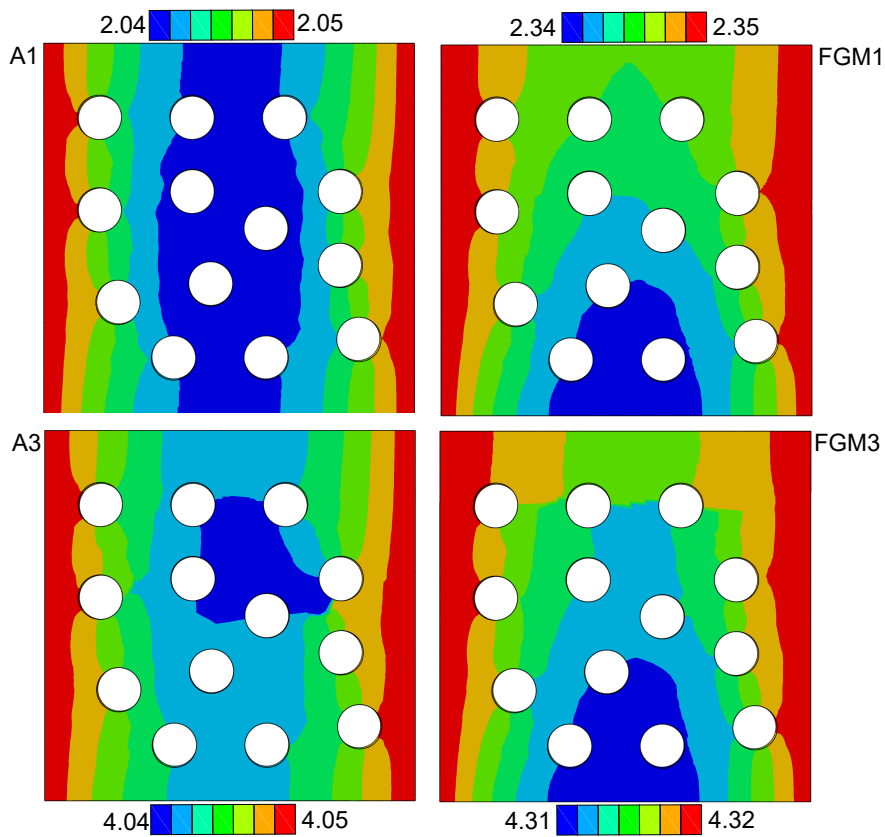
Figure 7: Plate with holes: temperature distribution in FGM as compared with that of the homogeneous model, before and after failure.
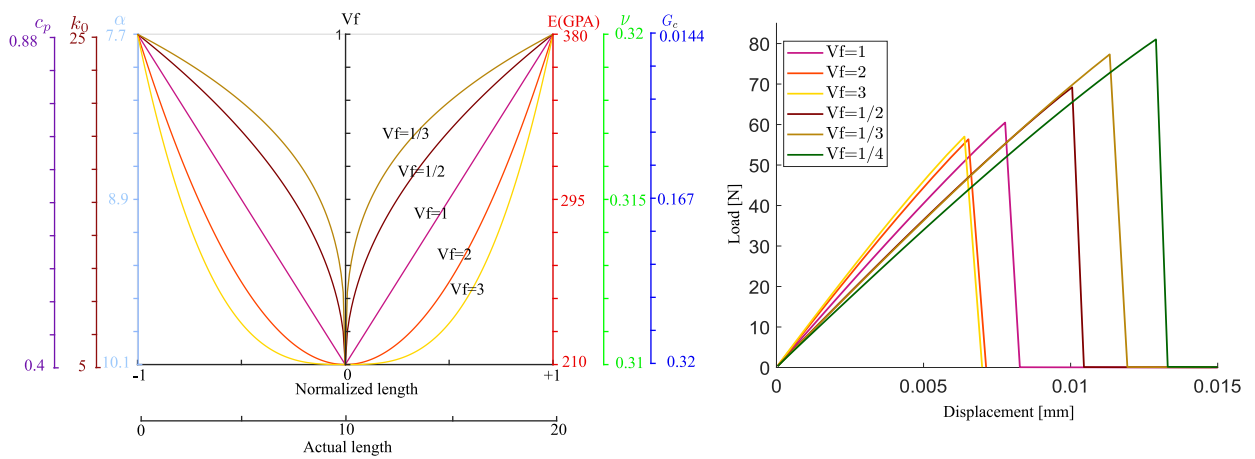
Figure 8: Cylinder with hole: properties of the materials and force vs displacement curve for change of grading function ζ.
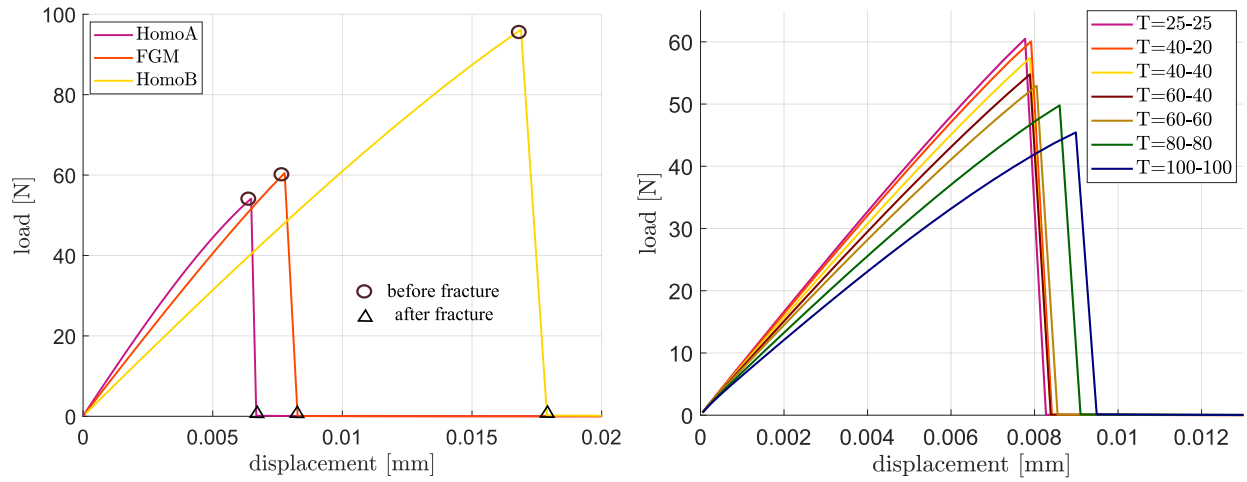
16

Figure 9: Cylinder with hole: force vs displacement curve FGM ($\zeta = 1$) and the Homogeneous surrogates and variation of temperature boundary conditions.
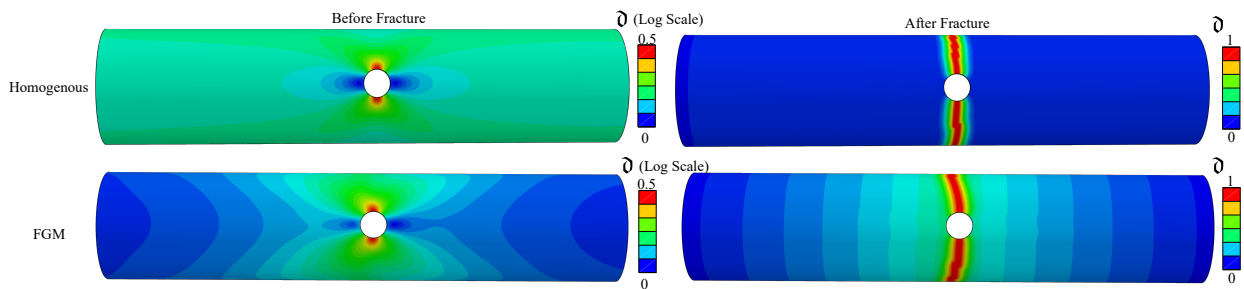

Figure 10: Cylinder with hole: phase-field and temperature distribution in FGM compared with homogeneous model before and after fracture.

elements. One axial end of the cylinder is restrained, whereas an axial displacement is prescribed on the opposite end. The initial temperature of $T = 25^oC$ is applied on both axial ends. The grading is done along its axial length ($z-$direction) such that the function Vf takes the form

$$Vf_A = \left(\frac{|z - 10|}{10}\right)^\zeta, \qquad 0 \le y \le \text{L}. \tag{38}$$

Meaning that, alumina occupies both the axial ends (i.e $z = 0$, and $z = 20$) and zirconia occupies the centre ($z = 10$). The grading profiles for different ζ, and the change of material properties due to the function Vf_A is shown in Fig. 8 (left panel). The force vs. displacement curves for the FGM, along with its homogeneous constituents, are shown in Fig. 9 (left panel). On the other hand, Fig. 8 (right panel) shows the variation of force vs displacement curve for different grading parameter ζ. It is evident that as $\zeta \to \infty$, the load-bearing capacity of the FGM approaches alumina (material-A) since the volume fraction of alumina is dense in the region of crack propagation.

Figure. 10 shows the comparison between crack paths for FGM and the homogeneous material (zirconia) and shows that the crack is deflected approximately 8° towards the load end. The variation of the temperature boundary conditions shows that as the temperature increases, the load-bearing capacity of the specimen decreases as in Fig. 9 (right panel).

Note that total energy can be fairly split into elastic, thermal, and crack energy constituents. Numerical experiments show that elastic energy is driven mainly by Young's Modulus, whereas a combination of $\mathbf{k}$ and α primarily drives thermal energy. In contrast, crack energy is largely driven by $\mathcal{G}_C$ and l_c in line with [48]. When the length scale of FGM is considered constant as in example-2, the crack energy is driven by $\mathcal{G}_C$. The crack propagation is usually towards the lowest $\mathcal{G}_C$ side (for example, alumina in the previous example). In the presence of stress concentrators such as a notch, hole, etc., the crack initiation and propagation also depends on the material properties at the stress concentration zones (crack tip). Since the variational formulation is considered as a competition between the thermo-elastic energy and the crack energy, the following conclusions can be readily drawn.

1. As the grading parameters increase, i.e ($\zeta \ge 1$) or decrease ($\zeta \le 1$), the FGM tends to behave like its homogeneous constituents.
2. As the temperature increases, the maximum load bearing capacity decreases.
3. The slope of the force vs. displacement curve depends strongly on the Young's modulus E.
4. The maximum load bearing capacity depends largely on $\mathcal{G}_C$, and it is directly proportional to l_c (or to the apparent tensile strength σ_c).
5. Since the thermal conductance is degraded as a function of $\mathfrak{d}$, and the maximum load bearing capacity is a function of applied temperature and $g(\mathfrak{d})$.

4.5. Plate with notch

This example concerns with the effect of grading and their subsequent temperature effects by considering three different FGM pairs. As an example, (i) Copper-Titanium (Cu-Ti), (ii) Alumina-Zirconia (A-Z), and (iii) Silicon carbide- Polymer Glass (SiC-G), representing (i) metal-metal, (ii) ceramic-ceramic, and (iii) ceramic polymer pairs respectively are considered. In each of the example, the model is discritized with 4476 elements.

The properties of materials mentioned above are given in Tab. 1, whereas the ratio of Young's modulus, fracture energy, thermal conductivity, and length scale are given in Tab. 2. Here, material-A has the highest Young's modulus among the FGM pairs. i.e $E_A = \max(E_A, E_B)$, i.e Copper, alumina and SiC is their respective FGM pairs.

Note that the ratio of chosen pairs represents vastly different mechanical and thermal properties, each of them is discussed in the sequel. A plate of length $L = 10$ mm and width $w = 10$ mm with initial notch of 3 mm at the centre are considered with the displacement boundary conditions applied as in Fig. 11a) to simulate stable crack propagation. A temperature $T = 25^oC$ is applied on both sides for the numerical

18

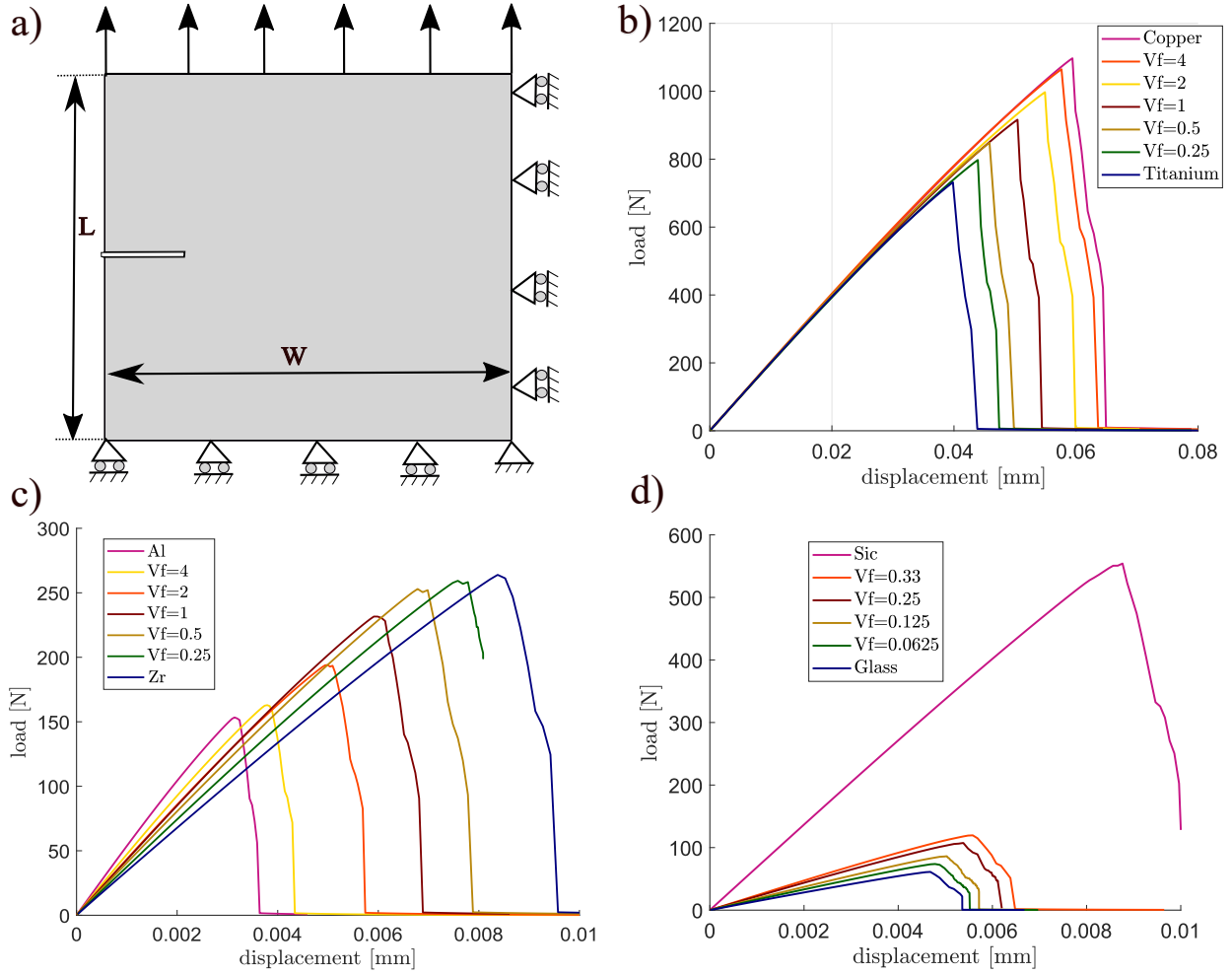Figure 11: a) Model under consideration, force vs displacement curve with variation of ζ in b) Copper-Titanium FGM pair, c) Alumina-Zirconia FGM pair, d) Silicon carbide-Epoxy glass FGM pair.

FGM pair	$\dfrac{E_A}{E_B}$	$\dfrac{\mathcal{G}_{c,A}}{\mathcal{G}_{c,B}}$	$\dfrac{k_{0,A}}{k_{o,B}}$	$\dfrac{l_{c,A}}{l_{c,B}}$
Copper-Titanium (Cu-Ti)	1.03	2	8.82	0.754
Alumina-Zirconia (A-Z)	1.8	0.207	4.95	1.33
Silicon Carbide- Polymer Glasss (SiC-G)	4.8	6.34	88.88	0.375

Table 2: ratio of the simulated materials.

19
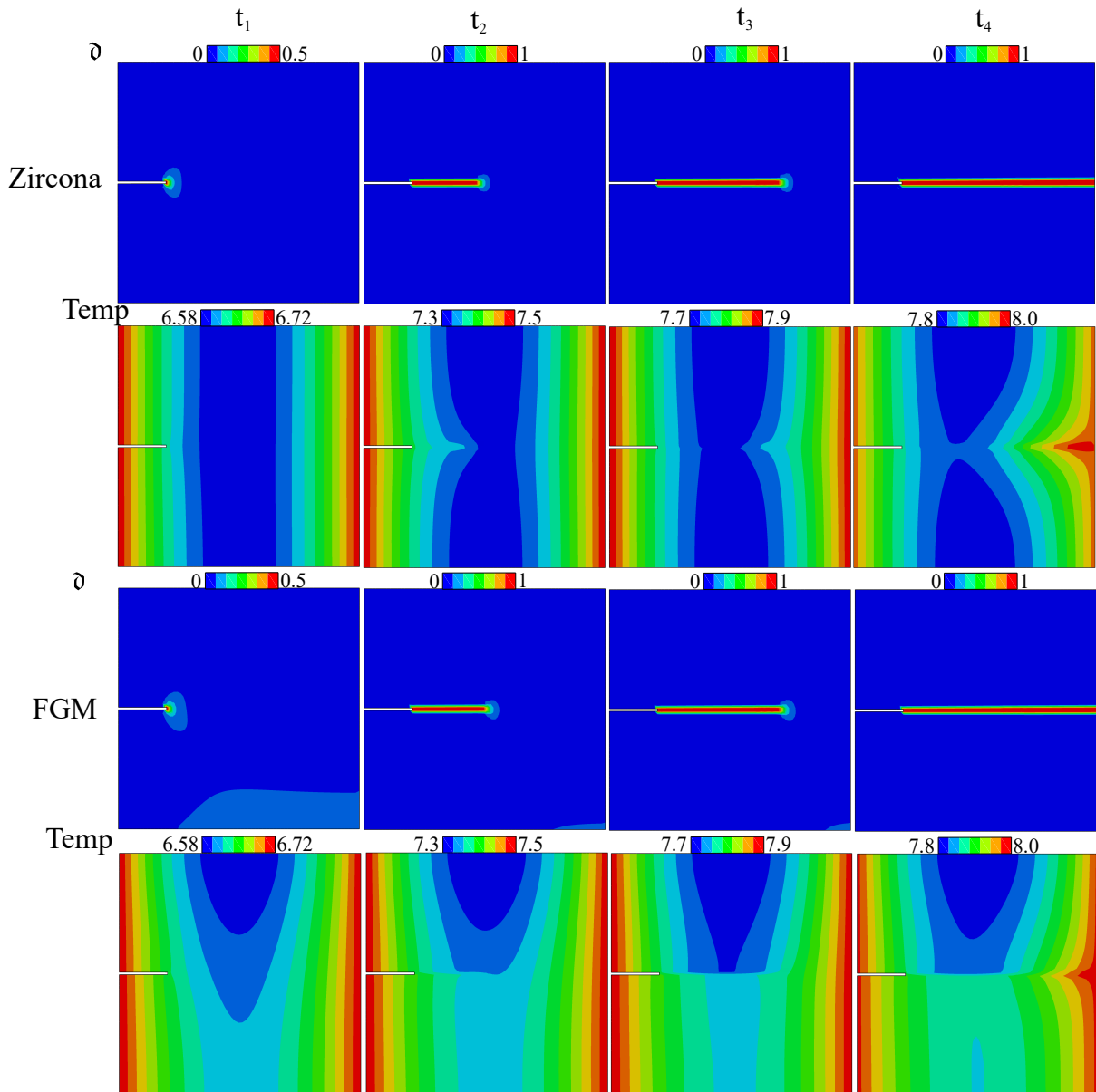
Figure 12: phase field and temperature distributions comparison between FGM and homogeneous material during (t_1) initiation, (t_2) crack propagation until 1/2 of plate (t_3) crack propagation until 3/4 of plate (t_4) after complete failure.

simulations in this example. The grading is done along the $y-$direction such that grading happens from the bottom (material-B) to top (material-A), whose function is defined as

$$V f_A = \left(\frac{y}{10}\right)^{\zeta} \quad 0 \leq y \leq L. \tag{39}$$

For the copper-titanium FGM pair with copper as material-A, Young's modulus ratio $\frac{E_A}{E_B}$ is approximately 1. The force vs. displacement curve for the FGM with different grading parameters ζ along with its homogeneous constituents are presented in Fig. 11(b). It is clear that the slope of all the curves is similar due to the similarity in the Young's moduli. Then, the peak load-bearing capacity of the model is driven by the $\mathcal{G}_C$ and l_c. In fact, using the expression, $l_c = \frac{27}{256} \frac{\mathcal{G}_C E}{\sigma_c^2}$, $\mathcal{G}_C$ and l_c can be directly related with σ_c. Note that both copper and titanium are highly conductive metals with a thermal conductance ratio $\frac{k_{0,A}}{k_{o,B}} = 8.82$, meaning that the temperature distribution is highly concentrated towards the Copper end.

For the alumina-zirconia pair, the Young's modulus ratio $\frac{E_A}{E_B}$ is approximately 2, whereas $\frac{k_{0,A}}{k_{o,B}} = 4.95$, Fig. 11(c) shows the force vs displacement curve for different grading parameters ζ. Moreover, Fig. 12 presents the crack propagation and temperature distribution of the homogeneous material (zirconia as an example) and FGM (with $\zeta = 1$) during four stages, namely (i) crack initiation, (ii) crack propagating approximately half the plate, (iii) crack propagating approximately $\frac{3}{4}^{th}$ of the plate, and finally (iv) fully cracked model. The temperature distribution at each of these stages is shown in Fig. 12 to comprehend the differences. As the crack propagates, the temperature around the crack increases, leaving a trail around the crack tips. Meanwhile, thermal conductance in the crack region approaches 0, hence creating thermal insulation around the region. Temperature distribution in all the FGM's are similar owing to the conductivity ratio always higher than 1 in all the pairs. See Fig. 12 for more details.

For the Silicon carbide and polymer glass FGM, the Young's Modulus ratio $\frac{E_A}{E_B}$ is approximately 5, whereas the $\frac{k_{0,A}}{k_{o,B}} = 88.88$, notice that, due to very high $\frac{\mathcal{G}_{C,A}}{\mathcal{G}_{C,B}}$ ratio, the FGM with $\zeta \geq 1$ gave a nonphysical boundary cracks, hence only $\zeta \leq 1$ is considered for the analysis. Fig. 11(d) shows the force vs. displacement curve for the FGM Sic-G along with its homogeneous constituents. From Fig. 11(a), (b), and (c), it is apparent that as Young's modulus ratio increases, the peak load-bearing capacity of the FGM changes drastically as a linear/nonlinear combination of their homogeneous constitutes.

4.6. Double FGM (three-phase FGM)

Double FGM is a three-phase functionally graded material where the material is graded with three different materials. This can also be considered as two functionally graded materials combined together at a point, see, [3] for more details. In order to accommodate such a model, the material parameters in Eq. (11) and (12) have to be modified accordingly.

Consider three materials, Mat-A, Mat-B and Mat-C. The volume fraction of each material at any position $\mathbf{x} \in \mathcal{B}_0$ can be written as $V f_A$, $V f_B$ and $V f_C$ such that $V f_A + V f_B + V f_C = 1$ for each $\mathbf{x} \in \mathcal{B}_0$. Introduce two grading parameters ζ_1 and ζ_2 that controls the behaviours of the grading in the materials. Then the volume fraction function for the FGM at any position vector can be defined as

$$V f = \begin{cases} V f_1(\mathbf{x}) & 0 \leq \mathbf{x} \leq (L_1, w_1, h_1) \\ V f_2(\mathbf{x}) & (L_1, w_1, h_1) \leq \mathbf{x} \leq (L_2, w_2, h_2), \end{cases} \tag{40}$$

for some length $(L_1, L_2) \leq L$, width $(w_1, w_2) \leq w$, and thickness $(h_1, h_2) \leq h$. The material properties now can be written as a function of $V f$. As an example, we consider the square plate with an initial notch as
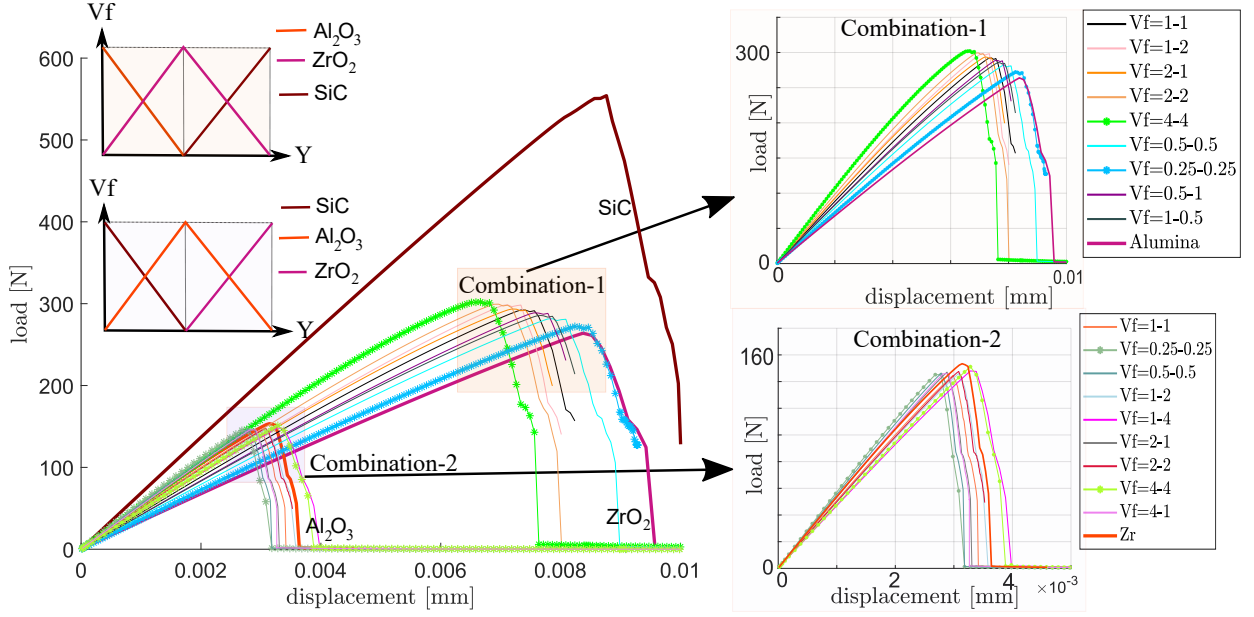
21

Figure 13: Force vs displacement curve for Double FGM.

in Sec. 4.5 with the same dimensions and boundary conditions. Alumina, zirconia, and silicon carbide are considered for the double FGM, where two combinations of grading of each of these materials to form a double FGM are considered in the $y-$direction are shown in Fig. 13.

The volume fraction functions can be defined as

$$Vf = \begin{cases} \left(\dfrac{y}{5}\right)^{\zeta_1} & 0 \leq y \leq 5 \\ \left(-\dfrac{y}{5}+2\right)^{\zeta_2} & 5 \leq y \leq 10, \end{cases} \tag{41}$$

The material properties now takes the form

$$\Xi = \begin{cases} \Xi_A + (\Xi_B - \Xi_A)\left(\dfrac{y}{5}\right)^{\zeta_1} & 0 \leq y \leq 5 \\ \Xi_C + (\Xi_B - \Xi_C)\left(-\dfrac{y}{5}+2\right)^{\zeta_2} & 5 \leq y \leq 10, \end{cases}$$

for each $\Xi = \{E, \nu, \alpha, k_0, \mathcal{G}_C, l_c\}$. Two combinations of the material properties are considered to explore the thermo-elastic behaviours of the double FGM's. In combination-1, zirconia is considered to exist everywhere across the model (coined as primary material). Meaning that, combination-1 can be considered as a two pairs of FGM of alumina-zirconia, zirconia-silicon carbide combined together with zirconia in both pairs. Similarly, combination-2, consists of silicon carbide-alumina, alumina-zirconia with alumina as a primary material. The choice of the materials is motivated by the fact that the E and k_0 ranges in the order of magnitude 1, whereas $\mathcal{G}_C$ ranges in the order of magnitude 2. The material properties of combination-1 can be written as

$$\Xi = \begin{cases} \Xi_{Alumina} + (\Xi_{zirconia} - \Xi_{Alumina})\left(\dfrac{y}{5}\right)^{\zeta_1} & 0 \leq y \leq 5 \\ \Xi_{SiC} + (\Xi_{zirconia} - \Xi_{SiC})\left(-\dfrac{y}{5}+2\right)^{\zeta_2} & 5 \leq y \leq 10, \end{cases}$$
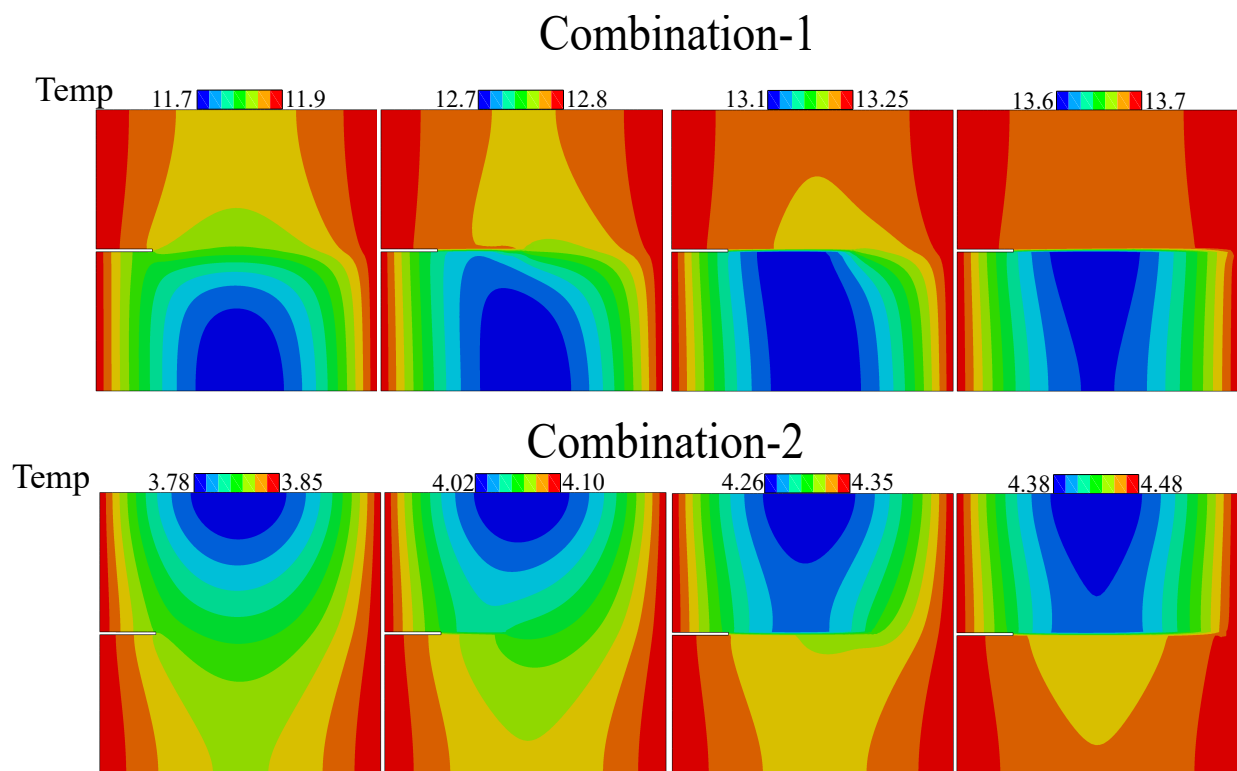
22

Figure 14: Temperature distribution between in combination-1 and combination-2 on different time instances for $\zeta = 1 - 2$ both.

whereas the material properties of combination-2 takes the form

$$\Xi = \begin{cases} \Xi_{SiC} + (\Xi_{Alumina} - \Xi_{SiC}) \left(\dfrac{y}{5}\right)^{\zeta_1} & 0 \leq y \leq 5 \\[2ex] \Xi_{Alumina} + (\Xi_{Alumina} - \Xi_{zirconia}) \left(-\dfrac{y}{5} + 2\right)^{\zeta_2} & 5 \leq y \leq 10, \end{cases}$$

Fig. 13 presents the pictorial representation of the combination-1 and combination-2 for $\zeta_1, \zeta_2 = 1$. For the different variations of the grading function ζ_1 and ζ_2 and the two combinations, the force vs. displacement curves can be seen in Fig. 13. It can be noticed that since the combination-1 is dominant with zirconia, the peak load response accumulates between the zirconia and the SiC. For combination-2, since alumina is dominant, the peak load responses are accumulated between alumina and zirconia. The temperature distribution for the combination-1 and combination-2 during the (i) crack initiation, (ii) crack propagating approximately half the plate, (iii) crack propagating approximately 3/4 of the plate, and finally (iv) fully cracked model is presented in Fig. 14. It is noticed that combination-2 has a faster rate of heat transfer compared to combination-1 owing to the thermal conductivity of alumina. And the temperature distributions are inclined towards the SiC in both combinations.

5. Concluding remarks

A thermodynamically consistent locking-free solid shell with full integration has been herein proposed for functionally graded materials. By the combination of 7 parameter shell elements, locking effects are alleviated. The numerical predicting capabilities of the model have been explored using several examples. The thermal conductivity degradation and the elastic energy degradation have been implemented using the same function $g(\mathfrak{d})$, although the formulation could be easily generalized by considering also different degradation functions.

An asymmetrical double-edge notched plate or with many holes have been analyzed to investigate the crack deflection in such complex FGM with all thermo-mechanical and fracture mechanics material properties function of space. The cylindrical shell example showed that the method can be effectively simulate crack deflection in FGM curved shells stemming from the material definition. The thermo-mechanical interaction and the difference between the elastic and temperature distribution between the FGM and homogeneous materials have been highlighted.

Furthermore, based on the representative examples, the model has been shown to predict that the temperature distributions affect crack growth patterns and, conversely, cracks do affect heat transfer since they create thermally insulated zones in the material.

A double FGM example has been also provided to show the possibility of combining two different FGM materials, which might be significant for material science.

Finally, it can be emphasized that the proposed model is promising in addressing a wide range of industrial applications dealing with thermo-elastic applications involving thin/thick (straight or curved) plates such as heat ex-changers, cutting tools, turbine blades, biomedical implants, heat-resisting elements in space crafts, sports equipment, etc., where FGMs are extensively used.

References

[1] A. Gupta, M. Talha, Recent development in modeling and analysis of functionally graded materials and structures, Progress in Aerospace Sciences 79 (2015) 1–14. doi:https://doi.org/10.1016/j.paerosci.2015.07.001.

[2] D. Jha, T. Kant, R. Singh, A critical review of recent research on functionally graded plates, Composite Structures 96 (2013) 833–849. doi:https://doi.org/10.1016/j.compstruct.2012.09.001.

[3] I. M. El-Galy, B. I. Saleh, M. H. Ahmed, Functionally graded materials classifications and development trends from industrial point of view, SN Applied Sciences 1 (11) (2019) 1378. doi:10.1007/s42452-019-1413-4.

[4] B. S. J. S. N. S. Bakar, W. Z. W., A. Sajjad, Functionally graded materials: An overview of dental applications, World Journal of Dentistry (2018) 137–144doi:https://doi.org/10.5005/jp-journals-10015-1523.

[5] M. Sato, A. Inoue, H. Shima, Bamboo-inspired optimal design for functionally graded hollow cylinders, PLOS ONE 12 (5) (2017) 1–14. doi:10.1371/journal.pone.0175029.

[6] N. Rödel.J, Gradient materials: An overview of a novel concept, Zeit Metall 88: 358-71. (1997).

[7] A. Moro, Y. Kuroda, K. Kusaka, Development status of the reusable high-performance engines with functionally graded materials, Acta Astronautica 50 (2002) 427–432. doi:10.1016/S0094-5765(01)00174-6.

[8] T. Guillén-Hernández, J. Reinoso, M. Paggi, Phase field model for fracture analysis of functionally graded power-based shell structures, Mechanics of Advanced Materials and Structures 0 (0) (2020) 1–11. doi:10.1080/15376494.2020.1751354.

[9] J. Reinoso, M. Paggi, C. Linder, Phase field modeling of brittle fracture for enhanced assumed strain shells at large deformations: formulation and finite element implementation, Computational Mechanics 59 (6) (2017) 981–1001. doi:10.1007/s00466-017-1386-3.
URL https://doi.org/10.1007/s00466-017-1386-3

[10] Niino.M, Hirai.T, Watanabe.R, The functionally gradient materials, Jap Soc Compos Mat 13: 257-64. (1987).

[11] B. Saleh, J. Jiang, A. Ma, D. Song, D. Yang, Effect of Main Parameters on the Mechanical and Wear Behaviour of Functionally Graded Materials by Centrifugal Casting: A Review, Metals and Materials International 25 (6) (2019) 1395–1409. doi:10.1007/s12540-019-00273-8.

[12] G. Udupa, S. S. Rao, K. Gangadharan, Functionally graded composite materials: An overview, Procedia Materials Science 5 (2014) 1291–1299, international Conference on Advances in Manufacturing and Materials Engineering, ICAMME 2014. doi:https://doi.org/10.1016/j.mspro.2014.07.442.

[13] F. Erdogan, Fracture mechanics of functionally graded materials, Composites Engineering 5 (7) (1995) 753 – 770. doi:https://doi.org/10.1016/0961-9526(95)00029-M.

[14] Z.-H. Jin, R. Batra, Some basic fracture mechanics concepts in functionally graded materials, Journal of the Mechanics and Physics of Solids 44 (8) (1996) 1221 – 1235. doi:https://doi.org/10.1016/0022-5096(96)00041-5.

[15] E. Martínez-Pañeda, On the finite element implementation of functionally graded materials., Materials (Basel, Switzerland) 12(2) (2019) 287. doi:10.3390/ma12020287.

[16] J. Reinoso, M. Paggi, R. Rolfes, A computational framework for the interplay between delamination and wrinkling in functionally graded thermal barrier coatings, Computational Materials Science 116 (2016) 82 – 95, articles from EUROMECH Colloquium 577 "Micromechanics of Metal Ceramic Composites". doi:https://doi.org/10.1016/j.commatsci.2015.08.031.
URL http://www.sciencedirect.com/science/article/pii/S0927025615005406

[17] M. Steigemann, M. Specovius-Neugebauer, M. Fulland, H. Richard, Simulation of crack paths in functionally graded materials, Engineering Fracture Mechanics 77 (11) (2010) 2145 – 2157. doi:https://doi.org/10.1016/j.engfracmech.2010.03.022.

[18] C. Comi, S. Mariani, Extended finite element simulation of quasi-brittle fracture in functionally graded materials, Computer Methods in Applied Mechanics and Engineering 196 (41) (2007) 4013 – 4026. doi:https://doi.org/10.1016/j.cma.2007.02.014.
URL http://www.sciencedirect.com/science/article/pii/S0045782507001697

[19] H. Bayesteh, S. Mohammadi, Xfem fracture analysis of orthotropic functionally graded materials, Composites Part B: Engineering 44 (1) (2013) 8 – 25. doi:https://doi.org/10.1016/j.compositesb.2012.07.055.
URL http://www.sciencedirect.com/science/article/pii/S1359836812005100

[20] Martínez-Pañeda, E. Gallego, Numerical analysis of quasi-static fracture in functionally graded materials, Int J Mech Mater Des 11 (2015) 405–424. doi:https://doi.org/10.1007/s10999-014-9265-y.

[21] N. S. S. Ooi, E.T., Crack propagation modelling in functionally graded materials using scaled boundary polygons, International journal of fracture 192 (2015) 87–105. doi:https://doi.org/10.1007/s10704-015-9987-3.

[22] K. D. Nguyen, H. Nguyen-Xuan, An isogeometric finite element approach for three-dimensional static and dynamic analysis of functionally graded material plate structures, Composite Structures 132 (2015) 423–439. doi:https://doi.org/10.1016/j.compstruct.2015.04.063.
URL https://www.sciencedirect.com/science/article/pii/S026382231500358X

[23] K. D. Nguyen, C.-L. Thanh, H. Nguyen-Xuan, M. Abdel-Wahab, A hybrid phase-field isogeometric analysis to crack propagation in porous functionally graded structures, Engineering with Computers (2021). doi:10.1007/s00366-021-01518-0.
URL https://doi.org/10.1007/s00366-021-01518-0

[24] C. Li, Z. Zou, Z. Duan, Multiple isoparametric finite element method for nonhomogeneous media, Mechanics Research Communications 27 (2) (2000) 137 – 142. doi:https://doi.org/10.1016/S0093-6413(00)00073-2.

[25] J.-H. Kim, G. Paulino, Isoparametric graded finite elements for nonhomogeneous isotropic and orthotropic materials, Journal of Applied Mechanics, Transactions ASME 69 (4) (2002) 502–514. doi:10.1115/1.1467094.

[26] Z. J. Zhang, G. H. Paulino, Cohesive zone modeling of dynamic failure in homogeneous and functionally graded materials,

International Journal of Plasticity 21 (6) (2005) 1195 – 1254, plasticity of Multiphase Materials. `doi:https://doi.org/10.1016/j.ijplas.2004.06.009`.

[27] Z.-H. Jin, G. Paulino, R. Dodds Jr., Finite element investigation of quasi-static crack growth functionally graded materials using a novel cohesive zone fracture model, Journal of Applied Mechanics, Transactions ASME 69 (3) (2002) 370–379. `doi:10.1115/1.1467092`.

[28] S. Kandula, J. Abanto-Bueno, P. Geubelle, J. Lambros, Cohesive modeling of dynamic fracture in functionally graded materials, Int J Fract 132 (3) (2005) 275–296.

[29] P. K. Kristensen, C. F. Niordson, E. Martínez-Pañeda, An assessment of phase field fracture: crack initiation and growth, Philosophical Transactions of the Royal Society A: Mathematical, Physical and Engineering Sciences 379 (2203) (2021) 20210021. `doi:10.1098/rsta.2021.0021`.

[30] B. Bourdin, G. Francfort, J.-J. Marigo, Numerical experiments in revisited brittle fracture, Journal of the Mechanics and Physics of Solids 48 (4) (2000) 797 – 826. `doi:https://doi.org/10.1016/S0022-5096(99)00028-9`.

[31] M. Dittmann, F. Aldakheel, J. Schulte, P. Wriggers, C. Hesch, Variational phase-field formulation of non-linear ductile fracture, Computer Methods in Applied Mechanics and Engineering 342 (2018) 71 – 94. `doi:https://doi.org/10.1016/j.cma.2018.07.029`.
URL `http://www.sciencedirect.com/science/article/pii/S0045782518303621`

[32] C. Miehe, D. Kienle, F. Aldakheel, S. Teichtmeister, Phase field modeling of fracture in porous plasticity: A variational gradient-extended eulerian framework for the macroscopic analysis of ductile failure, Computer Methods in Applied Mechanics and Engineering 312 (2016) 3 – 50, phase Field Approaches to Fracture. `doi:https://doi.org/10.1016/j.cma.2016.09.028`.
URL `http://www.sciencedirect.com/science/article/pii/S0045782516305412`

[33] A. Dean, S. Sahraee, J. Reinoso, R. Rolfes, A new invariant-based thermo-plastic model for finite deformation analysis of short fibre reinforced composites: Development and numerical aspects, Composites Part B: Engineering 125 (2017) 241–258.

[34] R. Alessi, F. Freddi, Phase-field modelling of failure in hybrid laminates, Composite Structures 181 (2017) 9 – 25. `doi:10.1016/j.compstruct.2017.08.073`.

[35] J. Bleyer, R. Alessi, Phase-field modeling of anisotropic brittle fracture including several damage mechanisms, Computer Methods in Applied Mechanics and Engineering 336 (2018) 213 – 236. `doi:https://doi.org/10.1016/j.cma.2018.03.012`.

[36] A. Quintanas-Corominas, J. Reinoso, E. Casoni, A. Turon, J. Mayugo, A phase field approach to simulate intralaminar and translaminar fracture in long fiber composite materials, Composite Structures (2019). `doi:10.1016/j.compstruct.2019.02.007`.

[37] A. Dean, J. Reinoso, N. Jha, E. Mahdi, R. Rolfes, A phase field approach for ductile fracture of short fibre reinforced composites, Theoretical and Applied Fracture Mechanics 106 (2020) 102495. `doi:https://doi.org/10.1016/j.tafmec.2020.102495`.
URL `http://www.sciencedirect.com/science/article/pii/S0167844219306536`

[38] F. Alkhatib, E. Mahdi, A. Dean, Development of composite double-hat energy absorber device subjected to traverser loads, Composite Structures 240 (2020) 112046. `doi:https://doi.org/10.1016/j.compstruct.2020.112046`.
URL `https://www.sciencedirect.com/science/article/pii/S0263822319345192`

[39] M. Brod, A. Dean, S. Scheffler, C. Gerendt, R. Rolfes, Numerical modeling and experimental validation of fatigue damage in cross-ply cfrp composites under inhomogeneous stress states, Composites Part B: Engineering 200 (2020) 108050. `doi:https://doi.org/10.1016/j.compositesb.2020.108050`.
URL `https://www.sciencedirect.com/science/article/pii/S1359836820306624`

[40] P. Asur Vijaya Kumar, A. Dean, J. Reinoso, M. Paggi, A multi phase-field-cohesive zone model for laminated composites: Application to delamination migration, Composite Structures 276 (2021) 114471. `doi:https://doi.org/10.1016/j.compstruct.2021.114471`.

[41] A. Dean, P. Asur Vijaya Kumar, J. Reinoso, C. Gerendt, M. Paggi, E. Mahdi, R. Rolfes, A multi phase-field fracture model for long fiber reinforced composites based on the puck theory of failure, Composite Structures 251 (2020) 112446. `doi:https://doi.org/10.1016/j.compstruct.2020.112446`.

[42] E. Martínez-Pañeda, A. Golahmar, C. F. Niordson, A phase field formulation for hydrogen assisted cracking, Computer Methods in Applied Mechanics and Engineering 342 (2018) 742 – 761. `doi:https://doi.org/10.1016/j.cma.2018.07.021`.
URL `http://www.sciencedirect.com/science/article/pii/S0045782518303529`

[43] M. Isfandbod, E. Martínez-Pañeda, A mechanism-based multi-trap phase field model for hydrogen assisted fracture, International Journal of Plasticity 144 (2021) 103044. `doi:https://doi.org/10.1016/j.ijplas.2021.103044`.

[44] C. Schreiber, R. Müller, C. Kuhn, Phase field simulation of fatigue crack propagation under complex load situations, Archive of Applied Mechanics 91 (2) (2021) 563–577. `doi:10.1007/s00419-020-01821-0`.

[45] K. Seleš, F. Aldakheel, Z. Tonković, J. Sorić, P. Wriggers, A general phase-field model for fatigue failure in brittle and ductile solids, Computational Mechanics 67 (5) (2021) 1431–1452. `doi:10.1007/s00466-021-01996-5`.

[46] P. Carrara, M. Ambati, R. Alessi, L. De Lorenzis, A framework to model the fatigue behavior of brittle materials based on a variational phase-field approach, Computer Methods in Applied Mechanics and Engineering 361 (2020) 112731. `doi:https://doi.org/10.1016/j.cma.2019.112731`.

[47] Z. Khalil, A. Y. Elghazouli, E. Martínez-Pañeda, A generalised phase field model for fatigue crack growth in elastic–plastic solids with an efficient monolithic solver, Computer Methods in Applied Mechanics and Engineering 388 (2022) 114286. `doi:https://doi.org/10.1016/j.cma.2021.114286`.

[48] P. Asur Vijaya Kumar, A. Dean, J. Reinoso, P. Lenarda, M. Paggi, Phase field modeling of fracture in functionally graded materials: γ-convergence and mechanical insight on the effect of grading, Thin-Walled Structures 159 (2021) 107234.

doi:https://doi.org/10.1016/j.tws.2020.107234.
URL https://www.sciencedirect.com/science/article/pii/S0263823120311046

[49] Hirshikesh, S. Natarajan, R. K. Annabattula, E. Martínez-Pañeda, Phase field modelling of crack propagation in functionally graded materials, Composites Part B: Engineering 169 (2019) 239–248. doi:https://doi.org/10.1016/j.compositesb.2019.04.003.
URL https://www.sciencedirect.com/science/article/pii/S135983681930229X

[50] J.-Y. Wu, V. P. Nguyen, C. T. Nguyen, D. Sutula, S. Sinaie, S. P. Bordas, Chapter one - phase-field modeling of fracture, Vol. 53 of Advances in Applied Mechanics, Elsevier, 2020, pp. 1–183. doi:https://doi.org/10.1016/bs.aams.2019.08.001.
URL https://www.sciencedirect.com/science/article/pii/S0065215619300134

[51] K. D. Nguyen, C. E.Augarde, W. M. Coombs, H. Nguyen-Xuan, M. Abdel-Wahab, Non-conforming multipatches for nurbs-based finite element analysis of higher-order phase-field models for brittle fracture, Engineering Fracture Mechanics 235 (2020) 107133. doi:https://doi.org/10.1016/j.engfracmech.2020.107133.
URL https://www.sciencedirect.com/science/article/pii/S0013794420307165

[52] K. D. Nguyen, C.-L. Thanh, F. Vogel, H. Nguyen-Xuan, M. Abdel-Wahab, Crack propagation in quasi-brittle materials by fourth-order phase-field cohesive zone model, Theoretical and Applied Fracture Mechanics 118 (2022) 103236. doi:https://doi.org/10.1016/j.tafmec.2021.103236.
URL https://www.sciencedirect.com/science/article/pii/S0167844221003311

[53] H. Nguyen-Xuan, G. Liu, S. Bordas, S. Natarajan, T. Rabczuk, An adaptive singular es-fem for mechanics problems with singular field of arbitrary order, Computer Methods in Applied Mechanics and Engineering 253 (2013) 252–273. doi:https://doi.org/10.1016/j.cma.2012.07.017.
URL https://www.sciencedirect.com/science/article/pii/S0045782512002393

[54] R. G. Tangella, P. Kumbhar, R. K. Annabattula, Hybrid phase-field modeling of thermo-elastic crack propagation, International Journal for Computational Methods in Engineering Science and Mechanics 0 (0) (2021) 1–16. doi:10.1080/15502287.2021.1904462.

[55] H. Badnava, M. A. Msekh, E. Etemadi, T. Rabczuk, An h-adaptive thermo-mechanical phase field model for fracture, Finite Elements in Analysis and Design 138 (2018) 31–47. doi:https://doi.org/10.1016/j.finel.2017.09.003.

[56] T.-T. Nguyen, D. Waldmann, T. Q. Bui, Computational chemo-thermo-mechanical coupling phase-field model for complex fracture induced by early-age shrinkage and hydration heat in cement-based materials, Computer Methods in Applied Mechanics and Engineering 348 (2019) 1–28. doi:https://doi.org/10.1016/j.cma.2019.01.012.

[57] A. Dean, J. Reinoso, S. Sahraee, R. Rolfes, An invariant-based anisotropic material model for short fiber-reinforced thermoplastics: Coupled thermo-plastic formulation, Composites Part A: Applied Science and Manufacturing 90 (2016) 186–199. doi:https://doi.org/10.1016/j.compositesa.2016.06.015.

[58] J. Dolbow, N. Moës, T. Belytschko, Modeling fracture in mindlin–reissner plates with the extended finite element method, International Journal of Solids and Structures 37 (48) (2000) 7161–7183. doi:https://doi.org/10.1016/S0020-7683(00)00194-3.
URL https://www.sciencedirect.com/science/article/pii/S0020768300001943

[59] S. Natarajan, P. Baiz, S. Bordas, T. Rabczuk, P. Kerfriden, Natural frequencies of cracked functionally graded material plates by the extended finite element method, Composite Structures 93 (11) (2011) 3082–3092. doi:https://doi.org/10.1016/j.compstruct.2011.04.007.
URL https://www.sciencedirect.com/science/article/pii/S0263822311001310

[60] P. M. A. Areias, T. Belytschko, Non-linear analysis of shells with arbitrary evolving cracks using xfem, International Journal for Numerical Methods in Engineering 62 (3) (2005) 384–415. doi:https://doi.org/10.1002/nme.1192.
URL https://onlinelibrary.wiley.com/doi/abs/10.1002/nme.1192

[61] P. Areias, J.-H. Song, T. Belytschko, Analysis of fracture in thin shells by overlapping paired elements, Computer Methods in Applied Mechanics and Engineering 195 (2006) 5343–5360.

[62] S. Forest, Micromorphic approach for gradient elasticity, viscoplasticity, and damage, Journal of Engineering Mechanics 135 (3) (2009) 117–131. doi:10.1061/(ASCE)0733-9399(2009)135:3(117).

[63] T. Waffenschmidt, C. Polindara, A. Menzel, S. Blanco, A gradient-enhanced large-deformation continuum damage model for fibre-reinforced materials, Computer Methods in Applied Mechanics and Engineering 268 (2014) 801–842. doi:https://doi.org/10.1016/j.cma.2013.10.013.

[64] R. H. J. PEERLINGS, R. DE BORST, W. A. M. BREKELMANS, J. H. P. DE VREE, Gradient enhanced damage for quasi-brittle materials, International Journal for Numerical Methods in Engineering 39 (19) (1996) 3391–3403. doi:https://doi.org/10.1002/(SICI)1097-0207(19961015)39:19<3391::AID-NME7>3.0.CO;2-D.

[65] A. Dean, S. Sahraee, K. Ozenc, J. Reinoso, R. Rolfes, M. Kaliske, A thermodynamically consistent framework to couple damage and plasticity microplane-based formulations for fracture modeling: development and algorithmic treatment, International Journal of Fracture 203 (2016) 115–134. doi:10.1007/s10704-016-0131-9.

[66] S. S. Shishvan, S. Assadpour-asl, E. Martínez-Pañeda, A mechanism-based gradient damage model for metallic fracture, Engineering Fracture Mechanics 255 (2021) 107927. doi:https://doi.org/10.1016/j.engfracmech.2021.107927.

[67] J. Kiendl, K.-U. Bletzinger, J. Linhard, R. Wüchner, Isogeometric shell analysis with kirchhoff–love elements, Computer Methods in Applied Mechanics and Engineering 198 (49) (2009) 3902–3914. doi:https://doi.org/10.1016/j.cma.2009.08.013.

[68] J. Kiendl, Y. Bazilevs, M.-C. Hsu, R. Wüchner, K.-U. Bletzinger, The bending strip method for isogeometric analysis of kirchhoff–love shell structures comprised of multiple patches, Computer Methods in Applied Mechanics and Engineering 199 (37) (2010) 2403–2416. doi:https://doi.org/10.1016/j.cma.2010.03.029.

27

[69] J. Kiendl, M.-C. Hsu, M. C. Wu, A. Reali, Isogeometric kirchhoff–love shell formulations for general hyperelastic materials, Computer Methods in Applied Mechanics and Engineering 291 (2015) 280–303. `doi:https://doi.org/10.1016/j.cma.2015.03.010`.

[70] An extended isogeometric thin shell analysis based on kirchhoff–love theory, Computer Methods in Applied Mechanics and Engineering 284 (2015) 265–291, isogeometric Analysis Special Issue. `doi:https://doi.org/10.1016/j.cma.2014.08.025`.

[71] S. Mostofizadeh, M. Fagerström, R. Larsson, Dynamic crack propagation in elastoplastic thin-walled structures: Modelling and validation, International Journal for Numerical Methods in Engineering 96 (2) (2013) 63–86. `doi:https://doi.org/10.1002/nme.4524`.
URL `https://onlinelibrary.wiley.com/doi/abs/10.1002/nme.4524`

[72] P. M. Areias, J. Song, T. Belytschko, Analysis of fracture in thin shells by overlapping paired elements, Computer Methods in Applied Mechanics and Engineering 195 (41) (2006) 5343–5360, john H. Argyris Memorial Issue. Part II. `doi:https://doi.org/10.1016/j.cma.2005.10.024`.
URL `https://www.sciencedirect.com/science/article/pii/S0045782505005475`

[73] G. Becker, C. Geuzaine, L. Noels, A one field full discontinuous galerkin method for kirchhoff–love shells applied to fracture mechanics, Computer Methods in Applied Mechanics and Engineering 200 (45) (2011) 3223–3241. `doi:https://doi.org/10.1016/j.cma.2011.07.008`.
URL `https://www.sciencedirect.com/science/article/pii/S0045782511002490`

[74] P. K. A. V. Kumar, A. Dean, S. Sahraee, J. Reinoso, M. Paggi, Non-linear thermoelastic analysis of thin-walled structures with cohesive-like interfaces relying on the solid shell concept, Finite Elements in Analysis and Design 202 (2022) 103696. `doi:https://doi.org/10.1016/j.finel.2021.103696`.
URL `https://www.sciencedirect.com/science/article/pii/S0168874X21001700`

[75] P. Asur Vijaya Kumar, A. Dean, J. Reinoso, M. Paggi, Nonlinear thermoelastic phase-field fracture of thin-walled structuresrelying on solid shell concepts: Theory and applications.

[76] W. Shu, I. Stanciulescu, Monolithic and staggered strategies using solid-shell formulations for nonlinear coupled thermoelasticity, Journal of Engineering Mechanics 145 (12) (2019) 04019095. `doi:10.1061/(ASCE)EM.1943-7889.0001669`.

[77] S. Klinkel, W. Wagner, A geometrical non-linear brick element based on the eas-method, International Journal for Numerical Methods in Engineering 40 (24) (1997) 4529–4545. `doi:https://doi.org/10.1002/(SICI)1097-0207(19971230)40:24<4529::AID-NME271>3.0.CO;2-I`.

[78] C. Miehe, A theoretical and computational model for isotropic elastoplastic stress analysis in shells at large strains, Computer Methods in Applied Mechanics and Engineering 155 (3) (1998) 193–233. `doi:https://doi.org/10.1016/S0045-7825(97)00149-7`.

[79] R. Hauptmann, K. Schweizerhof, A systematic development of 'solid-shell' element formulations for linear and non-linear analyses employing only displacement degrees of freedom, International Journal for Numerical Methods in Engineering 42 (1) (1998) 49–69. `doi:https://doi.org/10.1002/(SICI)1097-0207(19980515)42:1<49::AID-NME349>3.0.CO;2-2`.

[80] L. Svolos, H. M. Mourad, C. A. Bronkhorst, H. Waisman, Anisotropic thermal-conductivity degradation in the phase-field method accounting for crack directionality, Engineering Fracture Mechanics 245 (2021) 107554. `doi:https://doi.org/10.1016/j.engfracmech.2021.107554`.

[81] M. Bischoff, E. Ramm, Shear deformable shell elements for large strains and rotations, International Journal for Numerical Methods in Engineering 40 (23) (1997) 4427–4449. `doi:https://doi.org/10.1002/(SICI)1097-0207(19971215)40:23<4427::AID-NME268>3.0.CO;2-9`.

[82] J. Korelc, P. Wriggers, Consistent gradient formulation for a stable enhanced strain method for large deformations, Engineering Computations 13 (1) (1996) 103–123. `doi:10.1108/02644409610111001`.

[83] J. Simo, F. Armero, R. Taylor, Improved versions of assumed enhanced strain tri-linear elements for 3d finite deformation problems, Computer Methods in Applied Mechanics and Engineering 110 (3) (1993) 359–386. `doi:https://doi.org/10.1016/0045-7825(93)90215-J`.

[84] J. C. Simo, M. S. Rifai, A class of mixed assumed strain methods and the method of incompatible modes, International Journal for Numerical Methods in Engineering 29 (8) (1990) 1595–1638. `doi:https://doi.org/10.1002/nme.1620290802`.

[85] R. A. F. Valente, R. M. N. Jorge, R. P. R. Cardoso, J. M. A. César de Sá, J. J. A. Grácio, On the use of an enhanced transverse shear strain shell element for problems involving large rotations, Computational Mechanics 30 (4) (2003) 286–296. `doi:10.1007/s00466-002-0388-x`.

[86] P. Betsch, E. Stein, An assumed strain approach avoiding artificial thickness straining for a non-linear 4-node shell element, Communications in Numerical Methods in Engineering 11 (11) (1995) 899–909. `doi:https://doi.org/10.1002/cnm.1640111104`.

[87] E. N. Dvorkin, K. Bathe, A continuum mechanics based four-node shell element for general non-linear analysis, Engineering Computations 1 (1) (1984) 77–88. `doi:10.1108/eb023562`.

[88] L. Adam, J.-P. Ponthot, Thermomechanical modeling of metals at finite strains: First and mixed order finite elements, International Journal of Solids and Structures 42 (21) (2005) 5615–5655, pACAM VIII SPECIAL ISSUE. `doi:https://doi.org/10.1016/j.ijsolstr.2005.03.020`.

[89] R. P. R. Cardoso, J. W. Yoon, M. Mahardika, S. Choudhry, R. J. Alves de Sousa, R. A. Fontes Valente, Enhanced assumed strain (eas) and assumed natural strain (ans) methods for one-point quadrature solid-shell elements, International Journal for Numerical Methods in Engineering 75 (2) (2008) 156–187. `doi:https://doi.org/10.1002/nme.2250`.

[90] F. Gruttmann, W. Wagner, Structural analysis of composite laminates using a mixed hybrid shell element, Computational Mechanics 37 (6) (2006) 479–497. `doi:10.1007/s00466-005-0730-1`.

[91] E. P. Kasper, R. L. Taylor, A mixed-enhanced strain method: Part ii: Geometrically nonlinear problems, Computers & Structures 75 (3) (2000) 251–260. `doi:https://doi.org/10.1016/S0045-7949(99)00135-2`.

[92] L. Ambrosio, A. Braides, Energies in sbv and variational models in fracture mechanics. (1997).

[93] J. Reinoso, A. Blázquez, Application and finite element implementation of 7-parameter shell element for geometrically nonlinear analysis of layered cfrp composites, Composite Structures 139 (2016) 263–276. `doi:https://doi.org/10.1016/j.compstruct.2015.12.009`.

[94] H. Amor, J.-J. Marigo, C. Maurini, Regularized formulation of the variational brittle fracture with unilateral contact: Numerical experiments, Journal of the Mechanics and Physics of Solids 57 (8) (2009) 1209 – 1229. `doi:https://doi.org/10.1016/j.jmps.2009.04.011`.

[95] P. K. Kristensen, E. Martínez-Pañeda, Phase field fracture modelling using quasi-newton methods and a new adaptive step scheme, Theoretical and Applied Fracture Mechanics 107 (2020) 102446. `doi:https://doi.org/10.1016/j.tafmec.2019.102446`.

[96] Y. Navidtehrani, C. Betegón, E. Martínez-Pañeda, A simple and robust abaqus implementation of the phase field fracture method, Applications in Engineering Science 6 (2021) 100050. `doi:https://doi.org/10.1016/j.apples.2021.100050`.

[97] Z. Khalil, A. Y. Elghazouli, E. Martínez-Pañeda, A generalised phase field model for fatigue crack growth in elastic–plastic solids with an efficient monolithic solver, Computer Methods in Applied Mechanics and Engineering 388 (2022) 114286. `doi:https://doi.org/10.1016/j.cma.2021.114286`.